ORIGINAL RESEARCH ARTICLE

High-Resolution Mapping of Chromatin Conformation in Cardiac Myocytes Reveals Structural Remodeling of the Epigenome in Heart Failure

Editorial, see p 1626

BACKGROUND: Cardiovascular disease is associated with epigenomic changes in the heart; however, the endogenous structure of cardiac myocyte chromatin has never been determined.

METHODS: To investigate the mechanisms of epigenomic function in the heart, genome-wide chromatin conformation capture (Hi-C) and DNA sequencing were performed in adult cardiac myocytes following development of pressure overload–induced hypertrophy. Mice with cardiac-specific deletion of CTCF (a ubiquitous chromatin structural protein) were generated to explore the role of this protein in chromatin structure and cardiac phenotype. Transcriptome analyses by RNA-seq were conducted as a functional readout of the epigenomic structural changes.

RESULTS: Depletion of CTCF was sufficient to induce heart failure in mice, and human patients with heart failure receiving mechanical unloading via left ventricular assist devices show increased CTCF abundance. Chromatin structural analyses revealed interactions within the cardiac myocyte genome at 5-kb resolution, enabling examination of intra- and interchromosomal events, and providing a resource for future cardiac epigenomic investigations. Pressure overload or CTCF depletion selectively altered boundary strength between topologically associating domains and A/B compartmentalization, measurements of genome accessibility. Heart failure involved decreased stability of chromatin interactions around disease-causing genes. In addition, pressure overload or CTCF depletion remodeled long-range interactions of cardiac enhancers, resulting in a significant decrease in local chromatin interactions around these functional elements.

CONCLUSIONS: These findings provide a high-resolution chromatin architecture resource for cardiac epigenomic investigations and demonstrate that global structural remodeling of chromatin underpins heart failure. The newly identified principles of endogenous chromatin structure have key implications for epigenetic therapy.

Manuel Rosa-Garrido, PhD
Douglas J. Chapski, BS
Anthony D. Schmitt, PhD
Todd H. Kimball, BS
Elaheh Karbassi, PhD
Emma Monte, PhD
Enrique Balderas, PhD
Matteo Pellegrini, PhD
Tsai-Ting Shih, BS
Elizabeth Soehalim, BS
David Liem, MD, PhD
Peipei Ping, PhD
Niels J. Galjart, PhD
Shuxun Ren, MD
Yibin Wang, PhD
Bing Ren, PhD
Thomas M. Vondriska, PhD

Correspondence to: Thomas M. Vondriska, PhD, David Geffen School of Medicine, University of California, Los Angeles, BH 557 CHS, Department of Anesthesiology, 650 Charles Young Drive, Los Angeles, CA 90095. E-mail tvondriska@mednet.ucla.edu

Sources of Funding, see page 1623

Key Words: epigenomics ■ genomics ■ heart failure ■ hypertrophy

Clinical Perspective

What Is New?

- Chromatin capture and DNA sequencing were used to determine the endogenous structure of the cardiac myocyte epigenome.
- Physical interactions between regulatory elements and cardiac disease genes have been determined in basal and disease settings.
- The role of the chromatin structural protein CTCF was examined by using an in vivo loss-of-function model, revealing its role in chromatin organization and disease.

What Are the Clinical Implications?

- Epigenomic plasticity is identified as a common feature of cardiac pathophysiology induced by distinct stimuli.
- Knowledge of the dynamics of genomic interactions in disease may enable new strategies for therapeutic intervention.

Heart failure is a devastating condition that affects 6.5 million adults in the United States.[1] Although it is a multiorgan disease, heart failure is driven by changes in cardiac myocyte biology, including cell death, calcium handling, myofilament function, metabolism, and other factors. Underlying this complex cellular malfunction are gene expression changes, orchestrated by a network of transcription factors and chromatin-remodeling enzymes.[2–5] Despite this knowledge, the basic folding principles of the cardiac myocyte epigenome have never been revealed, and the role of chromatin structural changes in cardiovascular disease is unknown.

Correct packaging of the genome within the nucleus determines appropriate gene expression and cellular function.[6] Nucleosomes are differentially positioned along chromosomes, a process controlled by chromatin remodelers and histone-modifying enzymes.[7] Tracks of nucleosomes adopt fiberlike structures that in turn compose the 3-dimensional architecture of endogenous chromatin, a process that is necessary for orderly storage and controlled accessibility of genetic information.[8]

Chromatin modifications are engaged in a developmentally tuned manner to enable both the unidirectional procession of differentiation and transcriptome stability. Cells use enhancers,[9] distal regulatory regions that host histone posttranslational modifications and have an increasingly appreciated role in cardiovascular disease,[10–12] and chromatin-binding proteins that, together with transcription factors, sculpt the transcriptome. Among chromatin structural proteins, CTCF has been attributed a key role in modulating genome architecture[13] and maintaining regions of genome accessibility across cell types.[14] Once cellular lineages have been established, prevailing proteomic programs ensure that, on division, the correct epigenomic landscape is reestablished in daughter cells, maintaining lineage fidelity. An underexplored area of chromatin biology is how epigenomic stability is maintained in vivo when cells have exited the cell cycle. Adult mammalian cardiac myocytes do not readily divide, and the heart lacks robust regenerative capacity. Although epigenetic transitions in cardiovascular development have been investigated in cell culture,[15,16] much less is known about the adult heart. Previous studies have demonstrated a role for histone-modifying enzymes[3] and the readers of these modifications,[17] but whether 3-dimensional configuration of the genome contributes to heart disease remains to be determined.

Recent investigations have demonstrated the existence of topologically associating domains (TADs) as regions of chromatin that exhibit a higher level of local interactions. These structural neighborhoods of the genome may facilitate coregulation of gene expression and are shared across many biological conditions, suggesting they are fundamental features of the genome.[8,18] However, the specific nature of interactions within and between these TADs in cardiac cells, and the additional hierarchical levels of chromatin packaging (including local interactions, long-range interactions, enhancer-gene interactions, and chromatin looping) used in the cardiac myocyte nucleus in health and disease, are unknown.

The findings of the present study establish a high-resolution, genome-wide resource of endogenous chromatin interactions in cardiac myocytes, which can be used by future investigations to examine virtually any genomic locus. In addition, the results demonstrate specific areas of the epigenome that are structurally reorganized in pressure overload–induced heart disease, revealing how enhancers interact with disease-causing genes and the role of chromatin looping in cardiac gene expression. Using a physiologically relevant form of afterload-induced cardiac disease (plus a lineage targeted loss-of-function CTCF knockout [KO] mouse as a unique model for comparison), this investigation examines the role of global epigenome structure in heart failure.

METHODS

All animal studies were approved by the UCLA Animal Research Committee in compliance with the National Institutes of Health Guide for the Care and Use of Laboratory Animals. Human samples used in this study were procured in the Ronald Reagan Medical Center at UCLA following patient consent according to institutional review board–approved protocol. This study used DNA from adult mouse

Circulation. 2017;136:1613–1625. DOI: 10.1161/CIRCULATIONAHA.117.029430

cardiac myocytes isolated from control mice or 2 distinct disease models (pressure overload–induced hypertrophy and CTCF-KO) to perform chromosome conformation capture (Hi-C) analysis to determine endogenous chromatin structure (all sequencing-based studies were performed on n≥3 biological replicates per group; n values for all other end points are provided in figure legends). Transcriptome analyses were performed using RNA-seq to examine the functional readouts of any structural changes in the epigenome. Chromatin structure was then examined at multiple scales to determine structural units, hierarchical organization, and 3-dimensional regulation of accessibility and transcription.

Statistical Analyses

All sequencing-based studies were performed on n≥3 biological replicates per group; n values for all other end points are provided in figure legends. The statistical tests performed for each end point are listed in the individual figure legends, described in the Methods in the online-only Data Supplement and are summarized here: Student's t test (see Figure 1A and 1E, Figures IIC, IIE, and IV in the online-only Data Supplement); Tukey test (see Figure 1C); Wilcoxon test (see Figure 2F); and Pearson correlation (Figure IIIB in the online-only Data Supplement). For RNA-seq data, Cuffdiff was used to determine differential gene expression and assign *P* values and *q* values for each gene. For interaction analyses, see Figure 4B through 4D and Figure 5, Fit-Hi-C was used to filter for *cis*-interactions with *q* value <0.01, which were then used to map interactions.

Detailed methodology for all experiments and analyses are available in the online-only Data Supplement.

RESULTS

Chromosome Conformation Capture

Chromatin was purified from isolated cardiac myocytes and subjected to chromosome conformation capture (Hi-C). Mappability of reads was 63% to 65% across experimental groups (Figure IA in the online-only Data Supplement) at a depth of sequencing enabling examination of interactions with 5-kb resolution (Figure IB in the online-only Data Supplement). No significant differences were observed across experimental groups in terms of number of interactions analyzed, and the run-to-run variability was low (Figure IC in the online-only Data Supplement). Unless otherwise noted in the figures, all control groups were from myocytes isolated from untreated adult wild-type mice (all mice used in this study are C57BL/6 background). With this high-resolution resource, one can explore the physical environment of virtually any genomic locus in the cardiac myocyte at multiple scales including topologically associating domains, A/B compartmentalization, chromatin looping, enhancer interactions, and gene interactions. Sequencing data have been uploaded to the National Center for Biotechnology Information with the GEO accession number GSE96693 and are publically available.

Loss of CTCF Causes Cardiomyopathy

A mouse line with inducible, cardiac myocyte-specific ablation of CTCF was generated. Mice with a *loxp* flanked *Ctcf* allele ($Ctcf^{flox/flox}$ mice) were crossed with mice expressing a transgenic tamoxifen-inducible Cre protein under the control of the α-myosin heavy chain promoter (MerCreMer mice). When administered tamoxifen in the diet for 5 weeks followed by 1 week on regular chow (Figure IIA, right, in the online-only Data Supplement), $Ctcf^{flox/flox}$-$MerCreMer^{+/-}$ mice display selective excision of the targeted region of the *Ctcf* gene (Figure IIB in the online-only Data Supplement) and exhibit a gradual loss of the transcript in isolated cardiac myocytes (Figure IIC in the online-only Data Supplement). Further depletion in CTCF levels was associated with poor survival (Figure IID in the online-only Data Supplement); as a control, treatment of $Ctcf^{wt/wt}$-$MerCreMer^{+/-}$ mice with tamoxifen had no sustained effect on cardiac function or morphology (Figure IIG through III in the online-only Data Supplement). The experimental mice, $Ctcf^{flox/flox}$-$MerCreMer^{+/-}$ animals treated with tamoxifen to induce CTCF depletion, had ≈80% reduction in CTCF protein levels (Figure IIF in the online-only Data Supplement) and are henceforth referred to as CTCF-KO mice. A separate cohort of wild-type mice were subjected to pressure overload stress (through surgical application of transverse aortic constriction [TAC][19]) which induces heart failure through clinically relevant pathophysiological adaptation.

Phenotypic examination of the CTCF-KO mice revealed a striking cardiomyopathy (Figure 1 and Figure IIG through III in the online-only Data Supplement). Loss of CTCF leads to impaired ejection fraction, left ventricular chamber dilation, and muscle hypertrophy at the organ and cell level (Figure 1A through 1C). The TAC mice, by contrast, also exhibit hypertrophy accompanied by more modest changes in both chamber size and ejection fraction, demonstrating that these animals (CTCF-KO and TAC mice) represent distinct pathophysiological models. Examining CTCF expression in a genetically heterogeneous population of wild-type mice revealed consistent downregulation following pathological stimuli and an inverse correlation with pathological measurements of heart size (Figure IIIA and IIIB in the online-only Data Supplement; it is interesting to note that CTCF protein and mRNA levels were unchanged after TAC [data not shown], further suggesting that these models of disease, although they share some phenotypic characteristics, have important molecular and pathophysiological distinctions). The time course for chamber dilation, diminished ejection fraction, and CTCF depletion in CTCF-KO mice were similar (Figure IIC and IIIH in the online-only Data Supplement), and agreed with that for pathological gene activation (Figure IV in the online-only Data Supplement). CTCF-

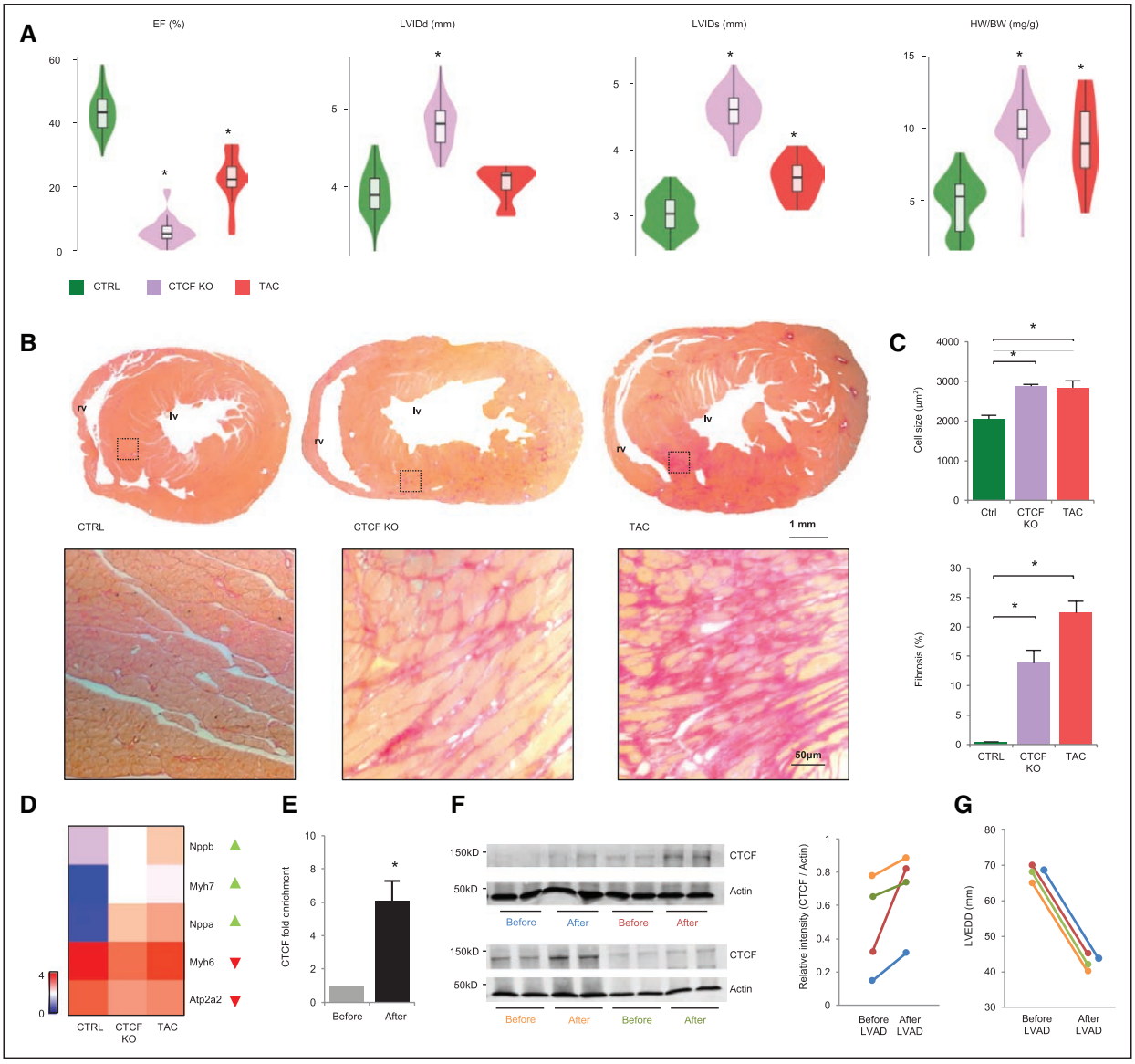

Figure 1. Loss of CTCF induces cardiac pathology.

A, Echocardiography measurements of ejection fraction (EF) and left ventricular internal diameter at diastole or systole (LVIDd or LVIDs) demonstrate impairment of EF and chamber dilation in CTCF-KO (purple) and TAC (red) in comparison with control (CTRL; green). Heart weight to body weight ratio (HW/BW) indicates cardiac hypertrophy in CTCF-KO and TAC mice (n≥25/group; **P*<0.01. Student's t test). **B,** Picrosirius red staining shows fibrosis after CTCF depletion or TAC (n=3/group). **C, Top,** mean cardiomyocyte area (n=20 visual fields of wheat germ agglutinin–stained sections across 3 mice per condition); **Bottom**, quantitation of fibrosis from Picrosirius red sections (n=3/group; **P*<0.01. Tukey HSD test). **D,** Stress response gene expression (log_{10}(FPKM+1)). **E,** Real-time qPCR measurements of CTCF levels in human myocardium before and after LVAD (before values normalized to 1 on a per-patient basis; n=4, **P*<0.01 Student's t test, bars SD). **F,** Western blots of CTCF levels in individual patients before and after LVAD (**Left**); quantitation of Western blots normalized to actin on a per-patient, per-sample basis (**Right**). **G,** Left ventricular end-diastolic dimension measurements before and after LVAD. Color-coding in **E** through **G** indicates separate patients. Lines shifted horizontally in **G** for ease of viewing. FPKM indicates fragments per kb of exon per million mapped reads; HSD, honest significant difference; KO, knockout; LVAD, left ventricular assist devices; qPCR, quantitative polymerase chain reaction; and TAC, transverse aortic constriction.

KO and TAC led to fibrotic deposition (Figure 1B, bottom) and activation of known heart failure genes[2] (Figure 1D; Figure ID in the online-only Data Supplement shows RNA-seq data quality statistics). Caspase-3 cleavage assays to measure apoptosis showed no difference between CTCF-KO and control animals (Figure V in the online-only Data Supplement, suggesting, but not proving, that impairment of cardiac function is secondary to necrosis). In human heart tissues harvested before and after implantation of left ventricular assist

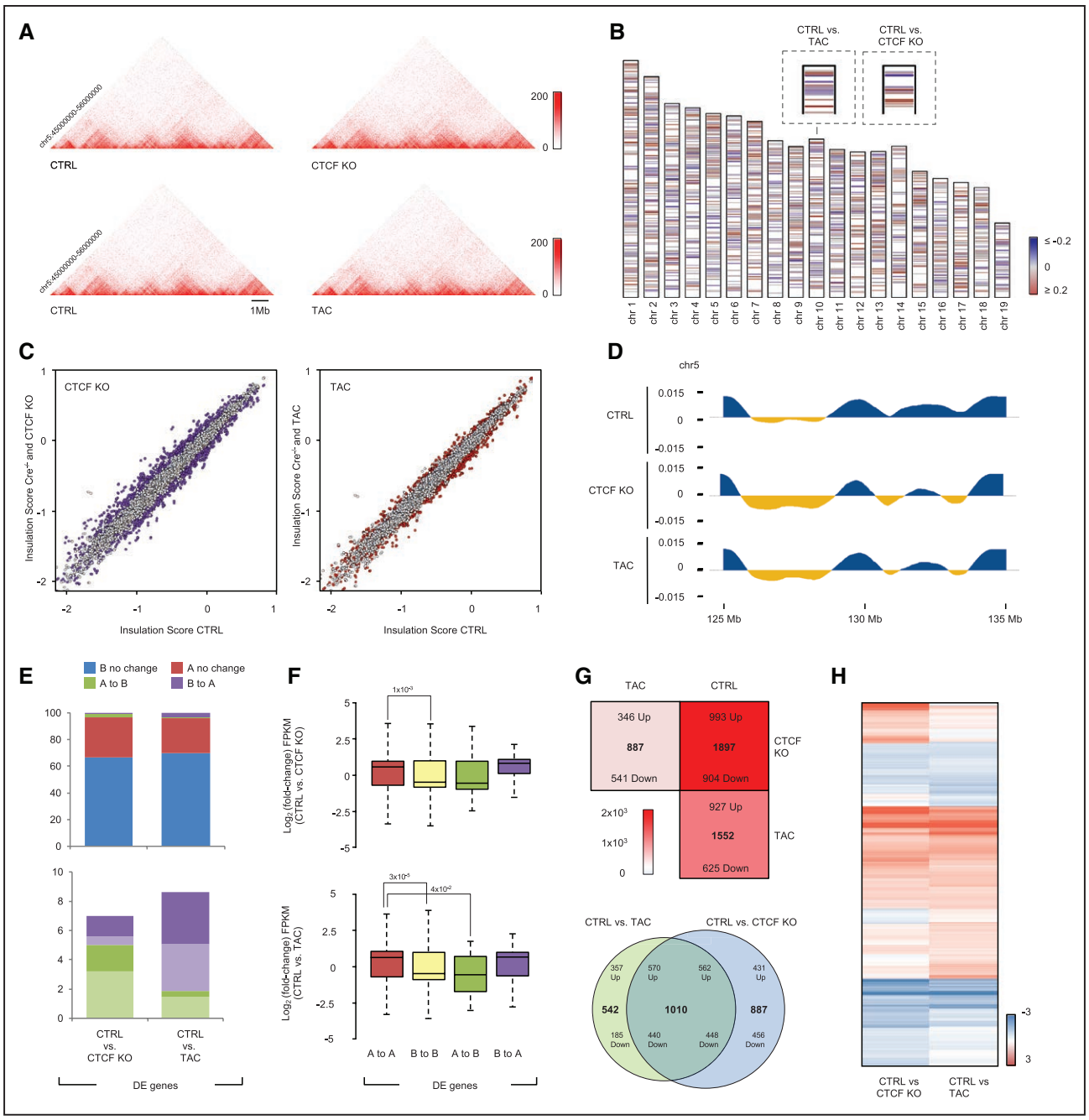

Figure 2. High-resolution cardiac chromatin conformation analyses reveal changes in chromatin compartmentalization and gene expression in pressure overload and CTCF-KO mice.

A, Structure of topological associating domains (TADs) is revealed from contact frequency heatmaps showing *cis*-interaction profile on example chromosome 5 for control, TAC, and CTCF-KO chromatin. **B,** Strength of boundaries between TADs are displayed for all chromosomes comparing control and TAC (red, higher; blue, lower; **Insets,** example region on chromosome 10 in control versus TAC and control versus CTCF-KO; Figure VIIA in the online-only Data Supplement shows control versus CTCF-KO for all chromosomes). **C,** Quantitation of insulation score differences in control versus KO (**Left**) or TAC (**Right**). Colored dots indicate significant changes (gray dots show range of variation between 2 control conditions: untreated wild-type mouse and untreated $Cre^{+/-}$ mouse). **D,** A/B compartmentalization, an indicator of genome accessibility at individual loci, for an example region on chromosome 5 is plotted in blue (open, A) and yellow (closed, B): CTRL A/B status on **Top**, CTCF-KO in **Middle**, and TAC on **Bottom**. **E,** Quantification of the genome-wide changes in A/B compartment change with CTCF depletion (**Left**) or TAC (**Right**). **Bottom** highlight only bins that change compartment; dark and light colors represent up- or downregulated genes, respectively. **F,** Relationship of compartmentalization to gene expression is measured in TAC or CTCF-KO hearts. Log_2(fold-change) of FPKM for the differentially expressed genes that either remain in the same compartment or that change compartments with CTCF depletion (**Top**) and TAC (**Bottom**). *P* values via Wilcoxon test; whiskers indicate (*Continued*)

devices, which mechanically unload the heart, allowing reverse remodeling of diseased tissue, CTCF levels were increased after device implantation (Figure 1E through 1G; see Figure VI in the online-only Data Supplement for patient clinical data; unavailability of healthy human hearts precluded the measurement of CTCF expression in these tissues).

Endogenous Chromatin Architecture in Healthy and Diseased Myocytes

We next aimed to examine the large-scale alterations in chromatin structure underlying heart disease in the mice subjected to TAC. There are several important differences in the pathophysiology between the CTCF-KO and TAC mice, and thus the former is used herein as a type of alternate disease model to investigate similarities and differences in global chromatin changes in different forms of heart failure. Analyses of TAD architecture in wild-type, CTCF-KO mice, or TAC mice demonstrate TADs to be stable features of chromatin structure (Figure 2A; average TAD size=445 kb). The number of TAD boundaries across the entire genome varied by <2%, with 3686, 3746, and 3705 boundaries called in control, CTCF-KO, and pressure overload, respectively. Boundary strength, however, was differentially altered across the genome (Figure 2B shows the distribution across chromosomes for control versus TAC; Figure 2C shows quantitation; Figure VIIA in the online-only Data Supplement shows all chromosomes in all conditions; Figure VIIIA in the online-only Data Supplement shows principal component analysis for boundary strength). CTCF-KO or TAC chromatin each hosted new boundaries (Figure VIIIB in the online-only Data Supplement; new includes shifted boundaries and de novo formation; note that the local rate of change in insulation score determines boundary strength[20]).

Chromatin can be divided into active and inactive regions,[21] called A and B compartments, respectively, which were affected to only a minor degree by loss of CTCF or TAC. Compartmentalization changes were sparse (Figure 2D and 2E) and ranged from <2 to ≈8% of interaction bins genome wide. The scale of the total genome changing compartmentalization was almost identical (≈4%) after CTCF-KO or TAC (Figure 2E). Changes in compartmentalization correlated positively with gene expression; that is, genes moving from A to B were downregulated and moving from B to A were upregulated (Figure 2F). Loss of CTCF elicited a transcriptional profile that shared some (41% of genes) features with TAC (Figures 2G and 2H; Figure VIIIC in the online-only Data Supplement shows principal component analysis of transcriptome data); both also exhibited known marker gene activation (Figure 1D). Genes determined by ChIP-seq to harbor CTCF in their transcription start sites were enriched in pathways associated with cardiac disease (Figure VIIID in the online-only Data Supplement).

Chromatin Looping Is Altered With CTCF-KO or TAC

The hierarchical nature of chromatin results in a preponderance of short-range interactions, while simultaneously necessitating long-range looping (Figure 3A). One such long-range interaction affected by CTCF depletion and TAC is shown in Figure 3B. Quantitative analysis shows that loss of CTCF or TAC was associated with a decrease in the total number of long-range loops, without a gross change in loop size (Figure 3C). Of dynamic loops in disease, 51% of those disappearing were shared between CTCF-KO and TAC, whereas only 15% of those appearing were shared; the raw number of loops lost in disease was also greater than the number formed (Figure 3D). In control chromatin, 37% (3056 of 8240; Figure 3E) of loops were flanked by 2 CTCF peaks (78% ≥1 peak) and loss of 1 CTCF peak was sufficient to destroy loops in 37% of the cases (326 of 879; Figure 3F). Within reorganized loops, enrichment for genes in pathways associated with cardiovascular function was observed (Figure VIIIE in the online-only Data Supplement; a caveat here is that analysis of cardiac myocytes may increase the chances that enriched ontology terms are of cardiovascular relevance).

Among total loops, a subset is responsible for bringing together enhancers and promoters (Figure 3G and 3H). In agreement with aberrant gene expression in both conditions (Figure 2F through 2H), lost loops in CTCF-KO and TAC chromatin were enriched in genes associated with cardiac pathology (Figure VIIIF in the online-only Data Supplement).

Heart Failure Involves Altered Enhancer-Gene Interactions

Focusing more deeply on significant interactions that contribute to gene expression can reveal the physiological implications of genomic structure. For example, *Ppp3ca*, a gene implicated in calcium-dependent signaling and cardiac hypertrophy,[4] exhibited a consistent

Figure 2 Continued. interquartile range. **G,** Heat matrix (**Top**) showing number of differentially expressed genes between CTRL, CTCF KO, and TAC (intensity indicates number of genes). Venn diagram (**Bottom**) showing overlap of differentially expressed genes between CTRL versus CTCF KO and CTRL versus TAC. **H,** Heatmap depicting $\log_2$(KO/CTRL) and $\log_2$(TAC/CTRL) FPKM for the differentially expressed genes with q<0.01 (**Left**). CTRL indicates control; FPKM, fragments per kb of exon per million mapped reads; KO, knockout; and TAC, transverse aortic constriction.

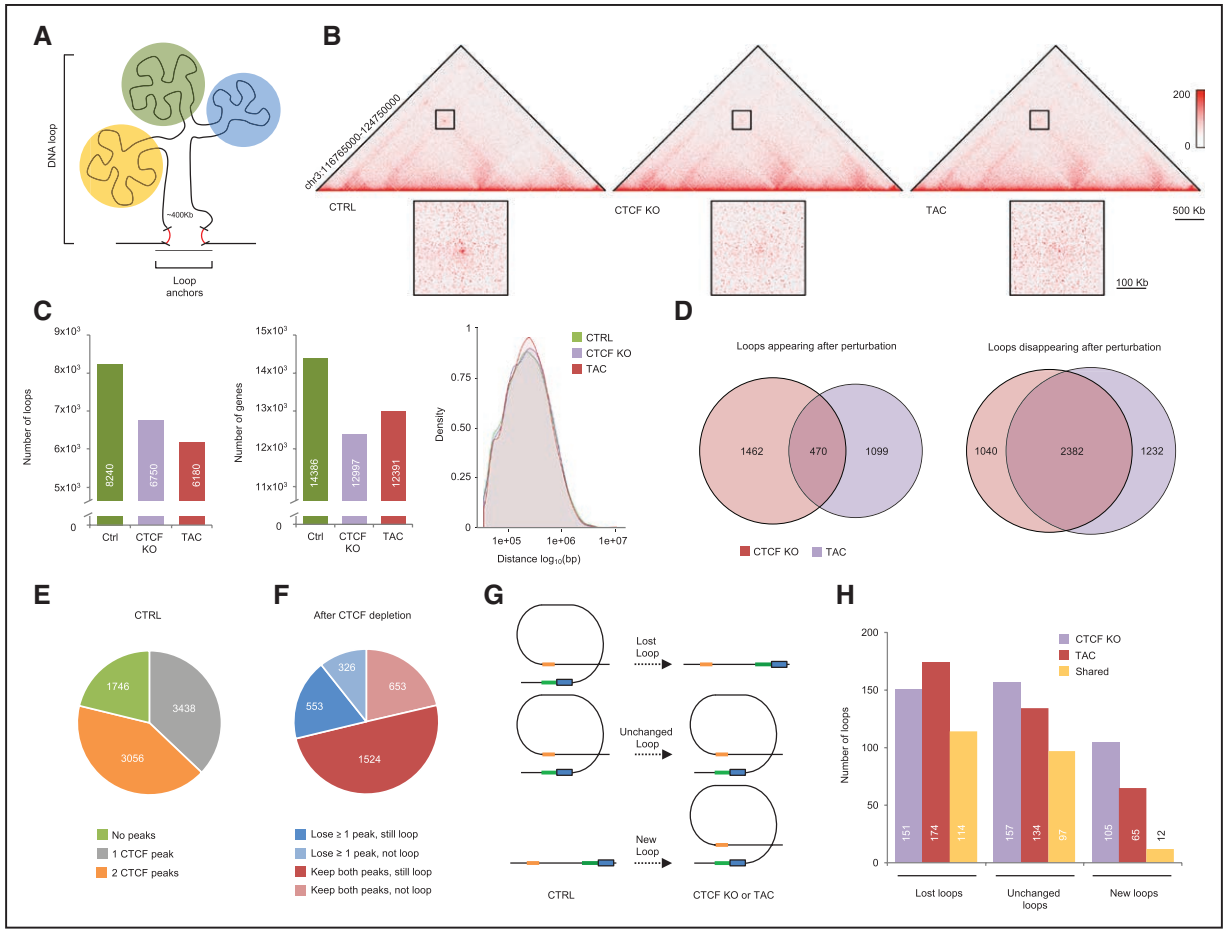

Figure 3. Short- and long-range chromatin interactions, and stable chromatin looping, are altered after pressure overload or CTCF-KO.

A, Schematic displaying that loops are demarcated by 2 anchors and contain regions of high-frequency interactions, indicated by the colored circles. **B,** The bioinformatic tool Juicebox is used to display an example loop that is lost with CTCF depletion (**Middle**) and TAC (**Right**). **C,** Quantitation of the phenomenon in **B** across genome, showing number of chromatin loops (**Left**), number of genes within loops (**Middle**), and loop sizes (**Right**; CTRL, green; CTCF-KO, purple; TAC, red). **D,** Overlap of loops only appearing in CTCF-KO or TAC in comparison with CTRL (**Left**); overlap of loops that disappear in CTCF-KO and TAC (**Right**). **E,** CTRL loops in which zero (green), one (gray), or both (yellow) anchors overlap with a CTCF peak. **F,** CTRL loops that lose ≥1 CTCF peak during CTCF depletion (blue) and CTRL loops that keep both CTCF peaks during CTCF depletion (red). Darker shade indicates loops that were preserved with CTCF depletion, whereas lighter color indicates loops that were lost. **G,** Schematic demonstrating types of alterations in looping architecture that can occur, including loss of loops mediating enhancer-promoter interactions (**Top**), no change (**Middle**), or formation (**Bottom**). Enhancers are orange, promoters green, and genes blue. **H,** Quantification of changes in enhancer-promoter loops. CTRL indicates control; KO, knockout; and TAC, transverse aortic constriction.

decrease in total interactions in CTCF-KO or TAC conditions (Figure 4A).

It is noteworthy that, of 9194 expressed genes for which significant (q<0.01) Fit-Hi-C data were available, 60% had the same direction of change of interactions in CTCF-KO and TAC conditions. Of the 40% of genes with unique behavior in the diseased condition, the majority (75%) were different because 1 of the 2 (CTCF-KO or TAC) exhibited no change in interaction; 25% were situations in which the change in interaction was opposite between CTCF-KO and TAC. Of the genes with shared changes in interactions in CTCF-KO and TAC that also underwent differential expression (3651 of 5443), the vast majority (86%) experienced decreased local interactions (Figure 4B). These findings support a trend in which more fluid chromatin interactions are associated with gene expression and where alterations in expression (when they occur) after perturbation are more likely to be in the same direction in CTCF-KO and TAC in contrast with control. Figure 4C shows the top 40 differentially expressed genes selected for the number of interactions in the control condition, demonstrating a consistent decrease in interactions in CTCF-KO and TAC.

Distinct mechanisms of gene regulation were associated with distinct changes in chromatin microenviron-

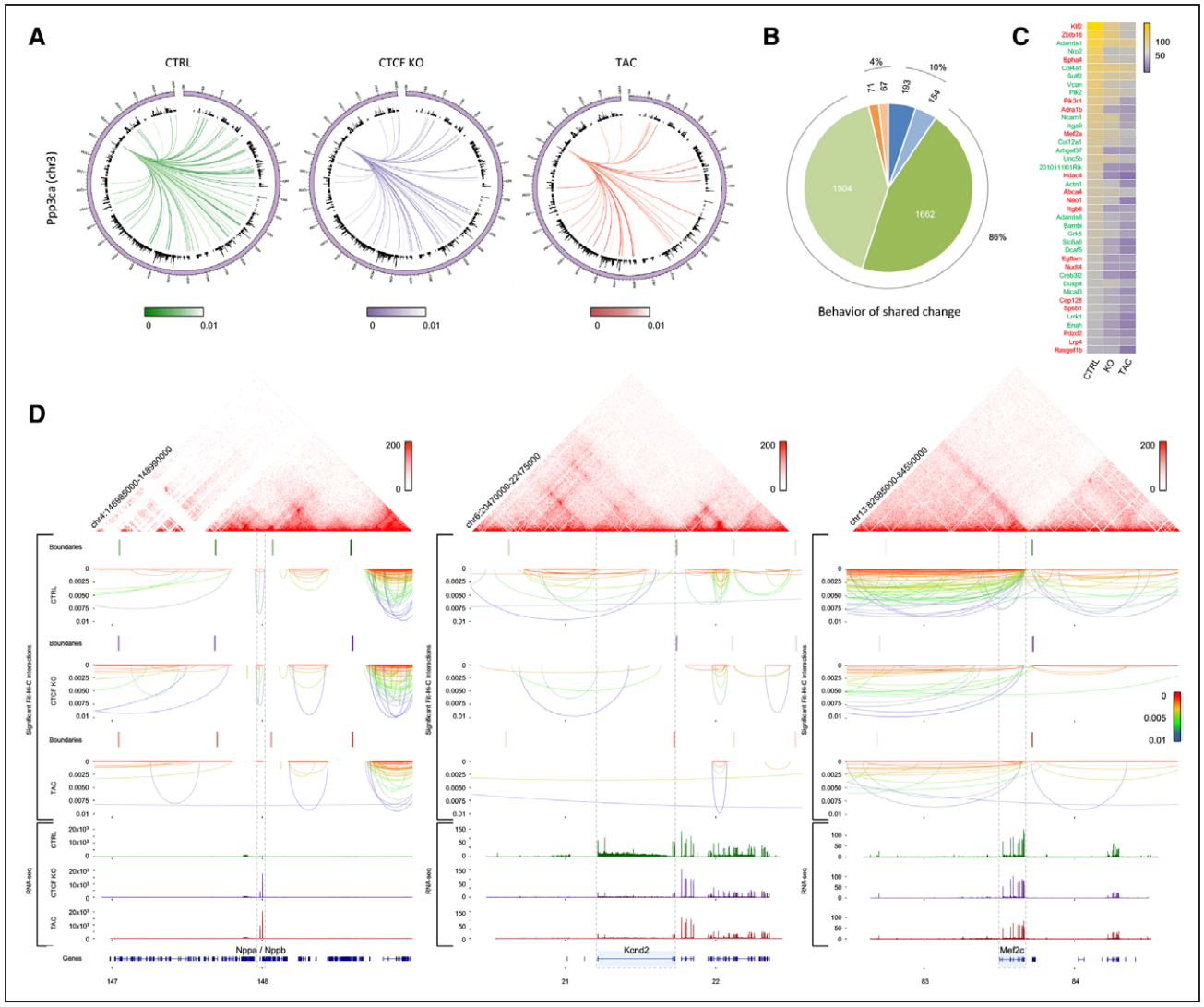

Figure 4. Chromatin architecture is remodeled around cardiac genes during disease.
A, As an example cardiac disease gene with changing long-range, intrachromosomal contacts, the sample-specific interactions emanating from *Ppp3ca* in control and after CTCF depletion or TAC are shown (q<0.01; 40-Kb resolution; outer circle, chromosome position; black, mm10 genes). **B,** Examining gene expression data for all 5443 genes with shared interaction behavior between CTCF-KO and TAC, 3651 genes were found to be differentially expressed in the same direction in perturbations in comparison with control. Most (86%) of these gene expression changes were associated with decreased chromatin interactions (green colors), with 1662 upregulated (dark green) and 1504 downregulated (light green). The remainder of the interaction changes (14%) were distributed between the other possible scenarios: increased interactions and expression (193, dark blue), increased interaction and decreased expression (154, light blue), no change in interactions and either an increase (71, dark orange) or decrease (67, light orange) in expression. **C,** Heatmap showing the number of significant (q<0.01) interactions overlapping with differentially expressed genes; top 40 shared differentially expressed genes shown, sorted by number of significant interactions in CTRL (gene name labeling shows direction of expression, where green is up and red is down). **D,** Higher-resolution mapping of local neighborhood interactions for the example genes *Nppa*/*Nppb*, *Kcnd2*, and *Mef2c* gene loci +/–1 Mb (q<0.01). Lines revealing precise contact sites are color coded by q-value significance, with red being the most significant. RNA-seq tracks depict gene expression for CTRL (green), CTCF-KO (purple), and TAC (red). CTRL indicates control; KO, knockout; and TAC, transverse aortic constriction.

ment, represented in 3 example genes (Figure 4D). Expression of *Nppa* (Figure 4D, left; the top is the control interaction matrix, the middle has specific interactions colored by significance, and the bottom has RNA-seq expression tracks), a known marker for heart failure in mice and humans,[2] was increased in CTCF-KO and TAC. Nearby local interactions are dense but relatively unchanging, whereas those impinging on the *Nppa* gene (demarcated by vertical lines) are decreased. Expression of *Kcnd2*, a potassium channel implicated in sudden death,[22] was downregulated, and the locus exhibited a notable decrease in long-range interactions in

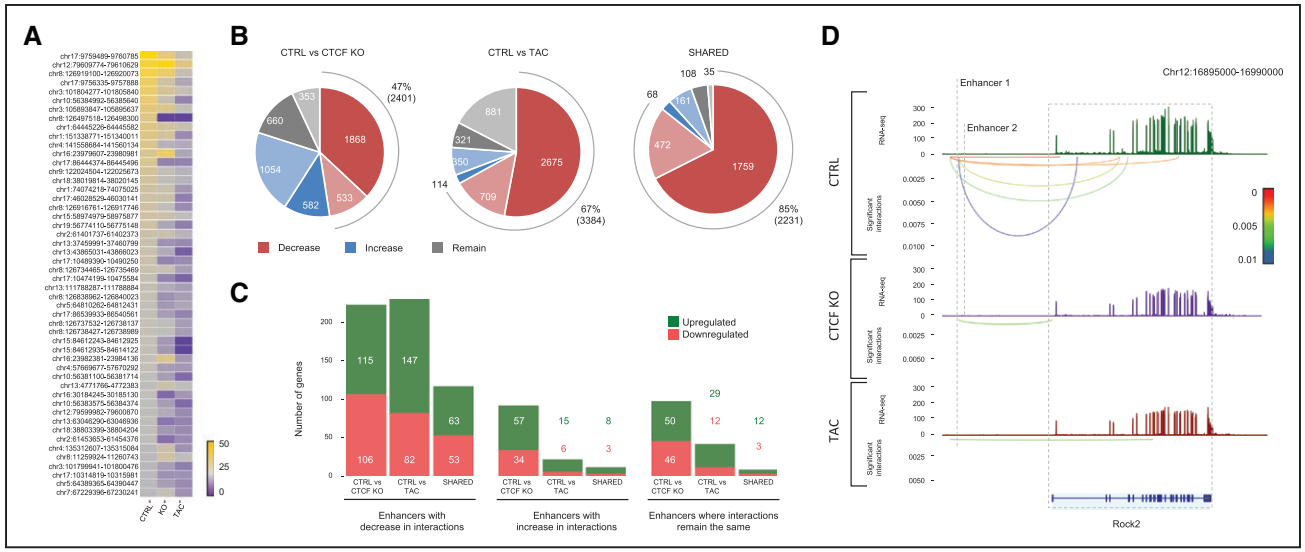

Figure 5. Three-dimensional interactions between enhancers and genes are restructured after pressure overload or CTCF-KO.

A, Number of contact sites per cardiac enhancer are quantified (q<0.01; rows are top 50 enhancers sorted by number of interactions). **B, Top,** enhancers in which the number of significant (q<0.01) interactions (determined by the Fit-Hi-C tool) increases (blue), decreases (red), or remains the same (gray) with CTCF-KO (**Left**), TAC (**Center**), and with consistent changes with CTCF-KO or TAC (**Right**). Darker shading indicates enhancers that interact with genes; lighter colors are regions not annotated as coding. **C,** Number of genes that interact with enhancers from **B**, stratified by whether their expression is upregulated (green) or downregulated (red). Groupings are separated into enhancers whose number of overlapping interactions decreases (**Left**), increases (**Middle**), or remains the same (**Right**) after perturbation. **D,** Contact site mapping of interactions is shown for the example gene *Rock2*, which exhibits decreased interaction with enhancers in CTCF-KO and TAC, concomitant with decreased expression. CTRL indicates control; KO, knockout; and TAC, transverse aortic constriction.

CTCF-KO and TAC (Figure 4D, center). Last, a third class of regulatory scheme is represented by *Mef2c*, whose expression changes with neither CTCF-KO nor TAC, but which undergoes a high degree of splicing regulation[23] and is a central driver of cardiac gene expression[24] (Figure 4D, right). This locus underwent a consistent decrease in chromatin interactions up- and downstream of the gene in CTCF-KO and TAC, suggesting a loosening of the local chromatin environment.

Enhancers are regions of the genome that positively influence gene expression and are identified on the basis of diagnostic histone posttranslational modifications. How enhancers are regulated in the 3-dimensional context of the cardiac nucleus is unknown. Of previously identified enhancers from adult cardiac myocytes,[11] 5050 contained significant Fit-Hi-C interactions. These enhancers consistently exhibited decreased interactions after perturbation (Figure 5A). Indeed, 47% of enhancers exhibited decreased interactions in CTCF-KO and 67% of enhancers exhibited decreased interactions in TAC (Figure 5B, left and center). It is remarkable that, of the enhancers that were shared between the 2 conditions, 85% showed a decrease of interactions in both CTCF-KO and TAC (Figure 5B, right). Figure 5C further illustrates that CTCF-KO and TAC were both associated with decreased enhancer-gene interactions (the directionality of gene expression change is reported in the different cohorts of enhancers from Figure 5B), and the affected genes were enriched in cardiac pathology pathways (Figure VIIIG in the online-only Data Supplement). *Rock2*, previously implicated in cardiac disease,[25] is an example gene whose interactions with multiple enhancers are depleted in the setting of CTCF-KO or TAC (Figure 5D; Tables I through III in the online-only Data Supplement). These findings indicate that a global increase in chromatin fluidity around enhancers is a shared feature of cardiac pathology.

DISCUSSION

This study provides a resource of endogenous chromatin architecture in cardiac myocytes and describes the global changes in chromatin interactions during heart failure. With these data, the basal microenvironment of any genomic locus can be explored in the future, and changes in this microenvironment can be examined in the setting of pressure overload–induced heart failure. As a model of heart disease caused by increased afterload (including hypertension and aortic stenosis), TAC was used in this study to investigate how global changes in the epigenome participate in disease pathogenesis; the CTCF-KO mouse was used as a complementary tool to investigate the role of a critical chromatin structural protein. It is interesting to

note that loss of CTCF or pressure overload–induced heart failure caused greater dynamics of endogenous chromatin structure and specific reorganization of enhancer-gene interactions. Depletion of CTCF resulted in a phenotype that shared some features of that induced by pressure overload (including fibrosis, hypertrophy, changes in ejection fraction, and changes in chamber dimensions), although there were notable differences between these phenotypes (particularly in the extent of left ventricular dilation), meaning that CTCF-KO does not fully recapitulate and is thus not a model of pressure overload hypertrophy, but rather, is a form of dilated cardiomyopathy with hypertrophy and fibrosis. Human patients with heart failure treated with left ventricular assist devices to unload the heart demonstrated increased CTCF protein and mRNA levels. Although this observation is interesting, caution is warranted in the extrapolation of these findings to the clinical arena: future cohort studies in cardiomyopathies of distinct etiology will be required to fully understand the role of CTCF in human heart failure.

Although the pattern of chromosome organization during mitosis is well known, how the genome is structured during interphase or in cells that have exited the cell cycle has remained a mystery until very recently. Interphase nuclei form chromosomal territories (features mainly characterized by microscopy),[26] which serve to segregate entire chromosomes apart from each other. The development of genome-wide DNA sequencing–based approaches in the past few years has enabled the precise determination of subchromosomal genome architecture.[8,18,27] This information, that is, how the genome is packaged in different cells, is important for basic science reasons (eg, to answer fundamental questions about the structure-function relationship between an invariant genome and a highly variable transcriptome [among different cells in a multicellular organism]) and for translational implications, as well (eg, many diseases involve changes in epigenetic machinery, but understanding how these chromatin modifiers exert their control of disease phenotype requires determination of the substrate on which they operate, ie, the structural conformation of the epigenome). With these considerations in mind, the present study investigates each of the various levels of hierarchical organization of cardiac chromatin including the formation of TADs and the compartmentalization of large swaths of the genome (Figure 2 and Figure VII in the online-only Data Supplement), intermediate structural features, including chromatin loops of various lengths (Figure 3), precise remodeling of interactions around genes involved in disease pathogenesis (Figure 4), and the structural organization of noncoding functional units (ie, enhancers, which incorporates existing knowledge of posttranslational modifications decorating histones at specific genomic loci) near the genes they modify (Figure 5).

The present study and previous work in the field suggest that heart failure is associated with a plastic epigenome (Figure 6): widespread changes in boundary strength (Figure 2C); decreased formation of chromatin loops (Figure 3C and 3D); decreased interactions in local chromatin environment of differentially expressed genes (Figure 4); and more fluid interactions between enhancers and genes (Figure 5). These findings support previous studies of heart failure showing global DNA demethylation,[28] altered histone stoichiometry and a decrease in heterochromatic posttranslational modifications,[19,29,30] activation of pathogenic noncoding RNAs,[31,32] and aberrant transcriptional activation.[3,4,33] Heart disease has been speculated to be the result of a reversion to more primitive gene expression programs[2]; the present findings extend this hypothesis, identifying shared epigenomic features in response to cellular stress.

Although CTCF has been associated with TAD boundaries,[34–36] its structural role has been unclear in postmitotic cells in vivo. The present study explores the role of CTCF in cardiac epigenome stability, but cannot unequivocally conclude whether CTCF is dispensable for TAD maintenance, insofar as residual CTCF was present. A recent investigation, using an auxin-inducible degron approach to deplete CTCF protein in mouse embryonic stem cells, demonstrated that near-

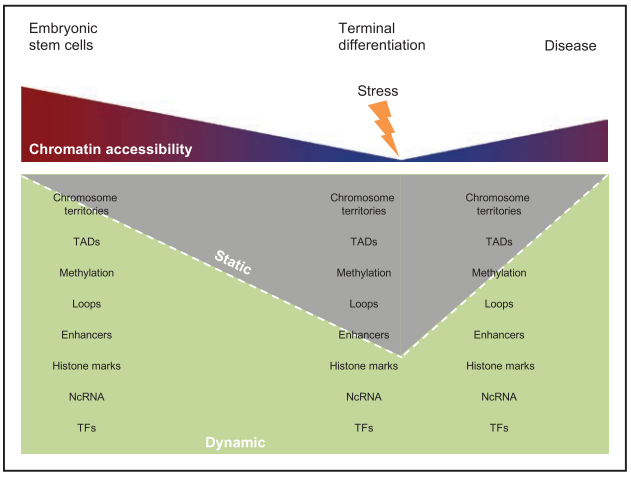

Figure 6. Model for epigenomic changes in development and disease.
Development is accompanied by changes in chromatin to endow terminally differentiated cells with stable transcriptomes. Disease upsets this balance, transitioning select regions of the genome into more dynamic conformations through effects on chromatin structure, enhancer-gene looping, histone modifications, DNA methylation, and other factors. This model is based on findings from this article and previous publications[2–5,10,11,15–17,29–33] as described in the text. NcRNA indicates noncoding RNA; TAD, topological associating domain; and TF, transcription factor.

complete depletion of CTCF was required to influence gross chromatin organization, with TAD structure still observed with as low as 4% of normal CTCF protein levels.[37] In the present article, because many loops did not harbor CTCF, and a large number of loops with unchanged CTCF binding were altered in their conformation, these findings support a model in which other factors stabilize chromatin looping and CTCF participates in gene regulation through mechanisms in addition to anchoring. Other insulator proteins (eg, cohesins, which behave similarly to CTCF across a population of mice and are modestly downregulated in CTCF-KO mice [Figure IIIA in the online-only Data Supplement], suggesting that cohesins and CTCF are coregulated in circumstances of global chromatin remodeling) may stabilize TADs, in addition to histone H3 lysine 27 trimethylation (globally unchanged in CTCF-KO, Figure IIF in the online-only Data Supplement) and perhaps DNA methylation. CTCF is essential for development beyond embryo implantation,[38] and longer-term depletion in the heart was lethal (Figure IID in the online-only Data Supplement). This investigation demonstrates that subtle perturbations in the structure of gene expression domains can result in catastrophic malfunction of the myocyte and heart, in agreement with previous findings implicating CTCF in disease-related transcription in other organs.[39] Cell death in the heart is an active area of investigation,[40] and, although our studies found no evidence for apoptotic cell death, it is possible, given the progressive nature of this phenotype, that the CTCF-KO cardiomyopathy is driven by more than one form of cell death to be determined in future studies. Our previous investigations[41] showed that CTCF knockdown was sufficient to induce cell death in HeLa cells but not in neonatal rat ventricular myocytes, and other investigations in noncardiac cells have suggested that aberrant CTCF function leads to abnormal cell death decisions, such as in cancer.[42]

Recent studies have identified a role for loops in the formation of chromatin neighborhoods to insulate against aberrant, and to coordinate synchronized, expression of genes.[43] In addition, ChIP-seq investigations of histone marks have provided important insights into how these features correlate with gene expression.[11] With high-resolution chromatin conformation data, the more biologically relevant approach can be taken to examine enhancers in the circumambient context in which they operate.[44] The present findings are a resource for examining gene regulation by virtually any known, or to-be-discovered, cardiac enhancer, and to explore newly identified 3-dimensional features of the cardiac nucleus.

In summary, these studies point to a common entropic destination for pathologically disturbed chromatin, supporting a model wherein chromatin structural abnormalities underpin the complex cellular networks that go awry in disease and providing a new conceptual framework to engineer therapies.

ACKNOWLEDGMENTS

The authors appreciate help from F. Ay and R. Tan (La Jolla Institute for Allergy and Immunology) with Fit-Hi-C, and Y. Qiu (Bing Ren laboratory) with Juicer. The authors thank A. J. Lusis and C. D. Rau (University of California, Los Angeles) for discussions and assistance. The authors thank the University of California, Los Angeles Center for Genomics for RNA-seq assistance. Author contributions: concepts, Drs Rosa-Garrido and Vondriska; methods, Dr Rosa-Garrido, D. J. Chapski, Drs Schmitt, Balderas, S. Ren, Pellegrini, B. Ren, and Vondriska; experiments, Dr Rosa-Garrido, D. J. Chapski, Dr Balderas, T.-T. Shih, E. Soehalim, Dr Karbassi, T. H. Kimball, Dr S. Ren; data analysis, Dr Rosa-Garrido, D. J. Chapski, Drs Schmitt, Monte, B. Ren, and Vondriska; writing, Dr Rosa-Garrido, D. J. Chapski, Dr Vondriska; revision and editing, all authors; resources, Drs Galjart, Liem, Ping, B. Ren, Wang, and Vondriska; funding acquisition, Drs Rosa-Garrido, Wang, and Vondriska.

SOURCES OF FUNDING

Dr Rosa-Garrido was supported by an American Heart Association Post-doctoral Fellowship (16POST27780019); D. J. Chapski was supported by the Eugene V. Cota-Robles Predoctoral Fellowship and a Ruth L. Kirschstein Institutional Training Grant (T32HL69766); Drs Karbassi and Monte were supported by American Heart Association Pre-doctoral Fellowships. This project was supported by the UCLA Cardiovascular Theme and National Institutes of Health grants HL 105699 (to Dr Vondriska), HL 115238 (to Dr Vondriska), and HL 129639 (to Drs Wang and Vondriska).

DISCLOSURES

None.

AFFILIATIONS

From Departments of Anesthesiology and Perioperative Medicine (M.R.-G., D.J.C., T.H.K., E.K., E.M., T.-T.S., E.S., S.R., Y.W., T.M.V.), Medicine (D.L., P.P., Y.W., T.M.V.), Physiology (P.P.,Y.W., T.M.V.), Molecular, Cellular and Developmental Biology (M.P.), UCLA, Los Angeles, CA; Nora Eccles Harrison Cardiovascular Research and Training Institute, University of Utah, Salt Lake City (E.B.); Ludwig Institute for Cancer Research, Department of Cellular and Molecular Medicine, Institute of Genomic Medicine, and Moores Cancer Center, UCSD, San Diego, CA (A.D.S., B.R.); and Department of Cell Biology and Genetics, Erasmus MC, Rotterdam, The Netherlands (N.J.G.).

FOOTNOTES

Received May 18, 2017; accepted July 31, 2017.

The online-only Data Supplement is available with this ar-

ticle at http://circ.ahajournals.org/lookup/suppl/doi:10.1161/CIRCULATIONAHA.117.029430/-/DC1.

Guest Editor for this article was Gerald Dorn II, MD.

Circulation is available at http://circ.ahajournals.org.

REFERENCES

1. Benjamin EJ, Blaha MJ, Chiuve SE, Cushman M, Das SR, Deo R, de Ferranti SD, Floyd J, Fornage M, Gillespie C, Isasi CR, Jiménez MC, Jordan LC, Judd SE, Lackland D, Lichtman JH, Lisabeth L, Liu S, Longenecker CT, Mackey RH, Matsushita K, Mozaffarian D, Mussolino ME, Nasir K, Neumar RW, Palaniappan L, Pandey DK, Thiagarajan RR, Reeves MJ, Ritchey M, Rodriguez CJ, Roth GA, Rosamond WD, Sasson C, Towfighi A, Tsao CW, Turner MB, Virani SS, Voeks JH, Willey JZ, Wilkins JT, Wu JH, Alger HM, Wong SS, Muntner P; American Heart Association Statistics Committee and Stroke Statistics Subcommittee. Heart Disease and Stroke Statistics-2017 Update: a report from the American Heart Association. *Circulation*. 2017;135:e146–e603. doi: 10.1161/CIR.0000000000000485.
2. Rajabi M, Kassiotis C, Razeghi P, Taegtmeyer H. Return to the fetal gene program protects the stressed heart: a strong hypothesis. *Heart Fail Rev*. 2007;12:331–343. doi: 10.1007/s10741-007-9034-1.
3. McKinsey TA, Olson EN. Dual roles of histone deacetylases in the control of cardiac growth. *Novartis Found Symp*. 2004;259:132–141; discussion 141.
4. Molkentin JD, Dorn GW 2nd. Cytoplasmic signaling pathways that regulate cardiac hypertrophy. *Annu Rev Physiol*. 2001;63:391–426. doi: 10.1146/annurev.physiol.63.1.391.
5. Kim SY, Morales CR, Gillette TG, Hill JA. Epigenetic regulation in heart failure. *Curr Opin Cardiol*. 2016;31:255–265. doi: 10.1097/HCO.0000000000000276.
6. Orphanides G, Reinberg D. A unified theory of gene expression. *Cell*. 2002;108:439–451.
7. Strahl BD, Allis CD. The language of covalent histone modifications. *Nature*. 2000;403:41–45. doi: 10.1038/47412.
8. Dekker J, Mirny L. The 3D genome as moderator of chromosomal communication. *Cell*. 2016;164:1110–1121. doi: 10.1016/j.cell.2016.02.007.
9. Heinz S, Romanoski CE, Benner C, Glass CK. The selection and function of cell type-specific enhancers. *Nat Rev Mol Cell Biol*. 2015;16:144–154. doi: 10.1038/nrm3949.
10. He A, Gu F, Hu Y, Ma Q, Ye LY, Akiyama JA, Visel A, Pennacchio LA, Pu WT. Dynamic GATA4 enhancers shape the chromatin landscape central to heart development and disease. *Nat Commun*. 2014;5:4907. doi: 10.1038/ncomms5907.
11. Papait R, Cattaneo P, Kunderfranco P, Greco C, Carullo P, Guffanti A, Viganò V, Stirparo GG, Latronico MV, Hasenfuss G, Chen J, Condorelli G. Genome-wide analysis of histone marks identifying an epigenetic signature of promoters and enhancers underlying cardiac hypertrophy. *Proc Natl Acad Sci USA*. 2013;110:20164–20169. doi: 10.1073/pnas.1315155110.
12. May D, Blow MJ, Kaplan T, McCulley DJ, Jensen BC, Akiyama JA, Holt A, Plajzer-Frick I, Shoukry M, Wright C, Afzal V, Simpson PC, Rubin EM, Black BL, Bristow J, Pennacchio LA, Visel A. Large-scale discovery of enhancers from human heart tissue. *Nat Genet*. 2011;44:89–93. doi: 10.1038/ng.1006.
13. Phillips JE, Corces VG. CTCF: master weaver of the genome. *Cell*. 2009;137:1194–1211. doi: 10.1016/j.cell.2009.06.001.
14. Schmitt AD, Hu M, Jung I, Xu Z, Qiu Y, Tan CL, Li Y, Lin S, Lin Y, Barr CL, Ren B. A compendium of chromatin contact maps reveals spatially active regions in the human genome. *Cell Rep*. 2016;17:2042–2059. doi: 10.1016/j.celrep.2016.10.061.
15. Wamstad JA, Alexander JM, Truty RM, Shrikumar A, Li F, Eilertson KE, Ding H, Wylie JN, Pico AR, Capra JA, Erwin G, Kattman SJ, Keller GM, Srivastava D, Levine SS, Pollard KS, Holloway AK, Boyer LA, Bruneau BG. Dynamic and coordinated epigenetic regulation of developmental transitions in the cardiac lineage. *Cell*. 2012;151:206–220. doi: 10.1016/j.cell.2012.07.035.
16. Paige SL, Thomas S, Stoick-Cooper CL, Wang H, Maves L, Sandstrom R, Pabon L, Reinecke H, Pratt G, Keller G, Moon RT, Stamatoyannopoulos J, Murry CE. A temporal chromatin signature in human embryonic stem cells identifies regulators of cardiac development. *Cell*. 2012;151:221–232. doi: 10.1016/j.cell.2012.08.027.
17. Haldar SM, McKinsey TA. BET-ting on chromatin-based therapeutics for heart failure. *J Mol Cell Cardiol*. 2014;74:98–102. doi: 10.1016/j.yjmcc.2014.05.002.
18. Dixon JR, Gorkin DU, Ren B. Chromatin domains: the unit of chromosome organization. *Mol Cell*. 2016;62:668–680. doi: 10.1016/j.molcel.2016.05.018.
19. Franklin S, Chen H, Mitchell-Jordan S, Ren S, Wang Y, Vondriska TM. Quantitative analysis of the chromatin proteome in disease reveals remodeling principles and identifies high mobility group protein B2 as a regulator of hypertrophic growth. *Mol Cell Proteomics*. 2012;11:M111.014258. doi: 10.1074/mcp.M111.014258.
20. Crane E, Bian Q, McCord RP, Lajoie BR, Wheeler BS, Ralston EJ, Uzawa S, Dekker J, Meyer BJ. Condensin-driven remodelling of X chromosome topology during dosage compensation. *Nature*. 2015;523:240–244. doi: 10.1038/nature14450.
21. Lieberman-Aiden E, van Berkum NL, Williams L, Imakaev M, Ragoczy T, Telling A, Amit I, Lajoie BR, Sabo PJ, Dorschner MO, Sandstrom R, Bernstein B, Bender MA, Groudine M, Gnirke A, Stamatoyannopoulos J, Mirny LA, Lander ES, Dekker J. Comprehensive mapping of long-range interactions reveals folding principles of the human genome. *Science*. 2009;326:289–293. doi: 10.1126/science.1181369.
22. Perrin MJ, Adler A, Green S, Al-Zoughool F, Doroshenko P, Orr N, Uppal S, Healey JS, Birnie D, Sanatani S, Gardner M, Champagne J, Simpson C, Ahmad K, van den Berg MP, Chauhan V, Backx PH, van Tintelen JP, Krahn AD, Gollob MH. Evaluation of genes encoding for the transient outward current (Ito) identifies the KCND2 gene as a cause of J-wave syndrome associated with sudden cardiac death. *Circ Cardiovasc Genet*. 2014;7:782–789. doi: 10.1161/CIRCGENETICS.114.000623.
23. Gao C, Ren S, Lee JH, Qiu J, Chapski DJ, Rau CD, Zhou Y, Abdellatif M, Nakano A, Vondriska TM, Xiao X, Fu XD, Chen JN, Wang Y. RBFox1-mediated RNA splicing regulates cardiac hypertrophy and heart failure. *J Clin Invest*. 2016;126:195–206. doi: 10.1172/JCI84015.
24. Martin JF, Schwarz JJ, Olson EN. Myocyte enhancer factor (MEF) 2C: a tissue-restricted member of the MEF-2 family of transcription factors. *Proc Natl Acad Sci USA*. 1993;90:5282–5286.
25. Okamoto R, Li Y, Noma K, Hiroi Y, Liu PY, Taniguchi M, Ito M, Liao JK. FHL2 prevents cardiac hypertrophy in mice with cardiac-specific deletion of ROCK2. *FASEB J*. 2013;27:1439–1449. doi: 10.1096/fj.12-217018.
26. Cremer T, Cremer C. Chromosome territories, nuclear architecture and gene regulation in mammalian cells. *Nat Rev Genet*. 2001;2:292–301. doi: 10.1038/35066075.
27. Bickmore WA, van Steensel B. Genome architecture: domain organization of interphase chromosomes. *Cell*. 2013;152:1270–1284. doi: 10.1016/j.cell.2013.02.001.
28. Greco CM, Kunderfranco P, Rubino M, Larcher V, Carullo P, Anselmo A, Kurz K, Carell T, Angius A, Latronico MV, Papait R, Condorelli G. DNA hydroxymethylation controls cardiomyocyte gene expression in development and hypertrophy. *Nat Commun*. 2016;7:12418. doi: 10.1038/ncomms12418.
29. Movassagh M, Choy MK, Knowles DA, Cordeddu L, Haider S, Down T, Siggens L, Vujic A, Simeoni I, Penkett C, Goddard M, Lio P, Bennett MR, Foo RS. Distinct epigenomic features in end-stage failing human hearts. *Circulation*. 2011;124:2411–2422. doi: 10.1161/CIRCULATIONAHA.111.040071.
30. Zhang QJ, Chen HZ, Wang L, Liu DP, Hill JA, Liu ZP. The histone trimethyllysine demethylase JMJD2A promotes cardiac hypertrophy in response to hypertrophic stimuli in mice. *J Clin Invest*. 2011;121:2447–2456. doi: 10.1172/JCI46277.
31. Chang CP, Han P. Epigenetic and lncRNA regulation of cardiac pathophysiology. *Biochim Biophys Acta*. 2016;1863(7 pt B):1767–1771. doi: 10.1016/j.bbamcr.2016.03.005.
32. Dorn GW 2nd, Matkovich SJ. Epitranscriptional regulation of cardiovascular development and disease. *J Physiol*. 2015;593:1799–1808. doi: 10.1113/jphysiol.2014.283234.
33. Sayed D, He M, Yang Z, Lin L, Abdellatif M. Transcriptional regulation patterns revealed by high resolution chromatin immunoprecipitation during cardiac hypertrophy. *J Biol Chem*. 2013;288:2546–2558. doi: 10.1074/jbc.M112.429449.
34. Giorgetti L, Lajoie BR, Carter AC, Attia M, Zhan Y, Xu J, Chen CJ, Kaplan N, Chang HY, Heard E, Dekker J. Structural organization of the inactive X chromosome in the mouse. *Nature*. 2016;535:575–579. doi: 10.1038/nature18589.
35. Dixon JR, Selvaraj S, Yue F, Kim A, Li Y, Shen Y, Hu M, Liu JS, Ren B. Topological domains in mammalian genomes identified by analysis of chromatin interactions. *Nature*. 2012;485:376–380. doi: 10.1038/nature11082.

36. Zuin J, Dixon JR, van der Reijden MI, Ye Z, Kolovos P, Brouwer RW, van de Corput MP, van de Werken HJ, Knoch TA, van IJcken WF, Grosveld FG, Ren B, Wendt KS. Cohesin and CTCF differentially affect chromatin architecture and gene expression in human cells. *Proc Natl Acad Sci USA*. 2014;111:996–1001. doi: 10.1073/pnas.1317788111.
37. Nora EP, Goloborodko A, Valton AL, Gibcus JH, Uebersohn A, Abdennur N, Dekker J, Mirny LA, Bruneau BG. Targeted degradation of CTCF decouples local insulation of chromosome domains from genomic compartmentalization. *Cell*. 2017;169:930–944.e22. doi: 10.1016/j.cell.2017.05.004.
38. Fedoriw AM, Stein P, Svoboda P, Schultz RM, Bartolomei MS. Transgenic RNAi reveals essential function for CTCF in H19 gene imprinting. *Science*. 2004;303:238–240. doi: 10.1126/science.1090934.
39. Tang Z, Luo OJ, Li X, Zheng M, Zhu JJ, Szalaj P, Trzaskoma P, Magalska A, Wlodarczyk J, Ruszczycki B, Michalski P, Piecuch E, Wang P, Wang D, Tian SZ, Penrad-Mobayed M, Sachs LM, Ruan X, Wei CL, Liu ET, Wilczynski GM, Plewczynski D, Li G, Ruan Y. CTCF-mediated human 3D genome architecture reveals chromatin topology for transcription. *Cell*. 2015;163:1611–1627. doi: 10.1016/j.cell.2015.11.024.
40. Kung G, Konstantinidis K, Kitsis RN. Programmed necrosis, not apoptosis, in the heart. *Circ Res*. 2011;108:1017–1036. doi: 10.1161/CIRCRESAHA.110.225730.
41. Monte E, Rosa-Garrido M, Karbassi E, Chen H, Lopez R, Rau CD, Wang J, Nelson SF, Wu Y, Stefani E, Lusis AJ, Wang Y, Kurdistani SK, Franklin S, Vondriska TM. Reciprocal regulation of the cardiac epigenome by chromatin structural proteins Hmgb and Ctcf: implications for transcriptional regulation. *J Biol Chem*. 2016;291:15428–15446. doi: 10.1074/jbc.M116.719633.
42. Oh S, Oh C, Yoo KH. Functional roles of CTCF in breast cancer (published online ahead of print June 26, 2017). *BMB Rep*. pii: 3893; PMID: 28648147. http://submit.bmbreports.org/Search/View.html?tmp_tr_num=3893. Accessed June 26, 2017.
43. Hnisz D, Day DS, Young RA. Insulated neighborhoods: structural and functional units of mammalian gene control. *Cell*. 2016;167:1188–1200. doi: 10.1016/j.cell.2016.10.024.
44. Spurrell CH, Dickel DE, Visel A. The ties that bind: mapping the dynamic enhancer-promoter interactome. *Cell*. 2016;167:1163–1166. doi: 10.1016/j.cell.2016.10.054.

High-Resolution Mapping of Chromatin Conformation in Cardiac Myocytes Reveals Structural Remodeling of the Epigenome in Heart Failure

Manuel Rosa-Garrido, Douglas J. Chapski, Anthony D. Schmitt, Todd H. Kimball, Elaheh Karbassi, Emma Monte, Enrique Balderas, Matteo Pellegrini, Tsai-Ting Shih, Elizabeth Soehalim, David Liem, Peipei Ping, Niels J. Galjart, Shuxun Ren, Yibin Wang, Bing Ren and Thomas M. Vondriska

Circulation. 2017;136:1613-1625; originally published online August 11, 2017;
doi: 10.1161/CIRCULATIONAHA.117.029430
Circulation is published by the American Heart Association, 7272 Greenville Avenue, Dallas, TX 75231

Print ISSN: 0009-7322. Online ISSN: 1524-4539

Supplemental Material

High resolution mapping of chromatin conformation in cardiac myocytes reveals structural remodeling of the epigenome in heart failure

Rosa-Garrido *et al*.

This section contains the extended Materials & Methods Section and Supplemental Figures 1-8. Supplemental Tables 1-3, containing enhancer-gene data, are uploaded as separate excel files. Sequencing data used in this paper have been deposited in NCBI with GEO accession number GSE96693.

MATERIALS & METHODS

Hi-C Methodology

For each replicate (n≥3 for all sequencing experiments in this paper), one million isolated adult cardiomyocytes were fixed in 1% formaldehyde and underwent *in situ* Hi-C as described,[1] using *MboI* as the restriction enzyme. Hi-C libraries were sequenced on an Illumina HiSeq 4000 instrument. Please see Figure S1 for detailed data on read counts, cis/trans interactions, and mappability. All sequencing data have been uploaded to NCBI with the GEO accession number GSE96693.

Bioinformatics Analyses of Hi-C Data

Raw paired-end 50bp reads were mapped to mm10 using BWA-MEM[2] as recently described.[3] Raw genome-wide contact matrices were generated using a custom Perl script. To normalize genome-wide raw contact matrices, we first removed bin pairs that fell outside the 5th and 99.5th percentiles (that had abnormally low or high coverage, respectively). We then used a custom Perl script to perform iterative correction and eigenvalue decomposition (ICE) on the filtered matrices for 50 iterations.[4] We then divided all entries in each genome-wide contact matrix by the corresponding matrix sum, and then multiplied them by the arbitrary value of 1 billion for 5kb resolution or 1 million for 40kb and 50kb resolution.[5] For the main analyses in this study, all biological replicates were combined.

For the individual replicate analyses, we generated replicate-specific contact matrices using the methods described above, and then calculated a Pearson correlation for the ice-corrected and normalized *cis* bin pairs for which we measured interactions in each replicate pair. We then plotted $\log_{10}$(normalized interactions) for each replicate on a respective axis using the smoothScatter() function in R. Once we determined a high correlation between replicates, we pooled the 3 replicates of each sample type together.

To generate 40kb z-score matrices, we first generated 40kb normalized contact matrices from the combined replicates for each sample type, using the methodologies described above. Z-score *cis* matrices were then generated using the loess method,[5] using the following function from the HiTC package[6] in Bioconductor: normPerExpected(matrix, method="loess", span=0.005, stdev=T). Then, *q*-values were calculated using the zscore2pval.R script in https://github.com/dekkerlab/cworld-dekker. Significant *q*-values < 0.01 were used for downstream analyses and Circos plot generation in R.

Identification of AB compartments at 5kb resolution was performed using the prcomp() function in R and correlating PC1 values to gene density. To generate a heatmap of difference in AB compartmentalization, we first determined the bins on autosomes that underwent compartment change in at least one sample. Then, we performed k-means clustering with $k = 5$. The AB difference graphs were generated using the following logic: If the PC1 value of a given bin of a diseased sample became more positive or less negative when compared to control, then the difference was deemed "positive" and the magnitude was shown in orange as a positive difference. Contrastingly, if the PC1 value of a given bin of a diseased sample became more negative or less positive, then the difference was deemed "negative" and the magnitude was shown in purple as a negative difference. To compare AB compartment changes with gene expression differences, we determined the AB compartmentalization for the TSS bin for each autosomal gene and then generated boxplots showing compartment change on the x-axis and $\log_2$(fold-change) of FPKM on the y-axis.

Insulation scores were calculated using the method,[5] using a 500kb sliding window across each 5kb normalized *cis* contact matrix. Insulation scores for all samples were normalized together using the normalize.quantiles() function of the preprocessCore package in Bioconductor (originally described[7]). The delta vector for each insulation score profile was generated using a custom R script, using a 500kb sliding window across each 5kb normalized contact matrix, and a 100kb outward distance to the left and right of each bin to calculate the

slope of the insulation score. Insulation boundaries were defined as local minima in the insulation score, and boundary strength was calculated. We discarded boundaries with strength < 0.1.[5] Insulation boundary heatmaps were generated by first calculating the insulation boundaries that overlap between control and CTCF knockout, and between control and TAC. Then, we generated heatmaps of overlapping boundary strength changes per autosome.

To call and visualize chromatin loops, we used Juicer[8] and Juicebox.[9] We first ran juicebox_tools_7.0 pre to generate .hic files for each condition, using reads with mapping quality ≥ 10. We then used juicebox_tools_7.0 hiccups, a functionality of Juicer, to call loops on the .hic files, using default parameters. Juicebox v1.5 was used to visualize the data. We then utilized the InteractionSet library [10] for custom downstream analyses.

Interaction Calling via Fit-Hi-C

To call significant interactions in our 5kb *cis* interaction matrices, we used the Bioconductor version of Fit-Hi-C (https://bioconductor.org/packages/release/bioc/html/FitHiC.html)[11] with the following parameters to analyze mid-range interactions up to 20Mb: distUpThresh=20000000, noOfBins=200. As input, we used concatenated raw autosomal 5kb *cis* interaction matrices and concatenated autosomal ICE bias vectors generated from our custom ICE implementation. After running Fit-Hi-C, we converted *cis* interactions with *q*-value < 0.01 into InteractionSet[10] format for interrogations of significant interactions using R.

Data Visualization

All visualizations of Hi-C data were generated either using custom R scripts written in house or using Juicebox.[9] For custom visualizations, we used the Bioconductor package ggbio.[12]

RNA-seq Methodology

Total RNA from isolated adult cardiomyocytes was isolated using the Qiagen RNeasy Mini Kit (Cat# 74104). RNA quality was assessed using the Agilent 2100 Bioanalyzer (Cat# G2940CA). Ribosomal RNA was then removed using an Illumina Ribo-Zero rRNA Removal Kit (Cat# MRZH11124) and the RNA-seq library was prepared at the UCLA Clinical Microarray Core using the KAPA Stranded RNA-Seq Library Preparation Kit (Cat# KK8401). The average insert size of each library was measured using an Agilent 4200 TapeStation (Cat# G2991AA). All libraries ranged from 200 to 400bp in length. RNA-seq libraries were sequenced on two lanes of an Illumina HiSeq 2000 to obtain 2x100bp (paired-end) reads. On average, ~50 million raw pairs were generated per library.

Bioinformatics Analyses of RNA-seq Data

Raw paired-end 100bp reads were sequenced on two lanes of an Illumina HiSeq 2000, and FASTQ files were demultiplexed using a custom Python script. Reads were mapped to the mm10 genome with TopHat v2.1.0,[13] using mm10 bowtie2 indices and a reference GTF provided by iGenomes (Illumina, downloaded from Ensembl release 81 on July 17, 2015). Transcripts were assembled using Cufflinks[14] v2.2.1 with the -G parameter (using the same GTF), and merged using the Cuffmerge feature of Cufflinks with the -g and -s parameters (using the same GTF and the reference FASTA provided by iGenomes, respectively).[14, 15] Cuffquant (from Cufflinks v2.2.1) was performed to determine transcript abundances for all samples, using the -b parameter (with reference FASTA from iGenomes), and the --max-bundle-frags 5000000 and -u parameters. Cuffdiff (also from Cufflinks v2.2.1) was used with identical extra parameters as Cuffquant to determine differential gene expression between conditions and assign *p*-values and *q*-values for each gene. Visualization of RNA-seq data was performed using cummerbund,[16] ggbio,[12] as well as custom R scripts.

ChIP-seq Methodology

ChIP for CTCF (Active Motif Cat# 61311) was performed on pooled isolated cardiomyocytes (~10 million total), using the ChIP-IT High Sensitivity Kit as described.[17] Cardiomyocyte pools were obtained from 3 control and 3 CTCF KO hearts. ChIP-seq libraries were prepared using the NuGEN Ovation Ultralow System V2 1–16 kit (Cat# 0344).

Bioinformatics Analyses of ChIP-seq Data

ChIP-seq libraries were sequenced on an Illumina HiSeq 2000 instrument. Raw single end 50 bp reads were demultiplexed using a custom Python script and then mapped to the same mm10 Ensembl reference genome as the RNA-seq data, but using Bowtie2[18] v2.2.6 with default parameters. Samtools[19] v0.1.19 was used to convert SAM files to BAM format, and peak calling was performed using the macs2.1.1.2016.0309 callpeak function[20] with default parameters. The CTCF ChIP BAM file was used as the treatment file and input BAM file as the control. A filtering step was added in R to only keep autosomal peaks.

ChIP-seq Visualizations

To visualize the distribution of CTCF peak occupancy across features of the mm10 genome, we used the ChIPseeker[21] package in Bioconductor. We used ngs.plot[22] to generate coverage heatmaps around TSSs and insulation boundaries.

KEGG Analysis

To determine the gene ontology of genes of interest, we used a custom R script that uses KEGG.db in Bioconductor,[23] with custom visualization.

Cardiomyocyte Isolation

Using an established protocol,[24] adult mice were treated with heparin (100 USP units) for 20 minutes to prevent blood coagulation, and then anesthetized with sodium pentobarbital (100μl of 50mg/ml dilution, intra-peritoneal). Upon loss of rear foot reflex, the heart was removed and instantaneously arrested in ice-cold phosphate buffered saline (PBS) and mounted on a modified Langendorff apparatus. After 5 min of perfusion with Tyrode's solution (130mM NaCl, 5.4mM KCl, 1mM MgCl2, 0.6mM Na2HPO4, 10mM glucose, and 10mM HEPES, pH 7.37, oxygenated with 95% (v/v) O_2-5% (v/v) CO_2) at 37°C, the heart was perfused for 15-30 min with 30 ml Tyrode's containing 20mg collagenase type-II and 3mg protease type-XIV and then washed for an additional 10 min with Krebs buffer (KB) (25mM KCl, 10mM KH2PO4, 2mM MgSO4, 20mM glucose, 20mM taurine, 5mM creatine, 100mM potassium glutamate, 10mM aspartic acid, 0.5mM EGTA, 5mM HEPES, pH 7.18) oxygenated with 95% O_2-5% (v/v) CO_2. Cardiomyocytes were dissociated in KB solution, filtered (100μm strainer) and centrifuged 2 min at 1000xg for further usage. This method obtained cells that were ≥95% cardiomyocytes by visual inspection of rod-shaped cell morphology.

Post-mortem histology, Cell Size Quantification and Fibrosis Detection

Whole hearts were rapidly excised from animals, perfused with 0.1 M potassium (K+) solution, fixed using 4% paraformaldehyde and then embedded in paraffin. Hearts were sectioned into 4μm thick sections. Cell size was determined using NIS-Elements Advanced Research v4.0, on heart slices labeled with wheat germ agglutinin (Thermo Fisher Scientific Cat# W11262). Fibrotic tissue was visualized using the Abcam Picrosirius Red Stain Kit (Cat# ab150681).

CTCF Knockout Mouse Generation

Ctcf-floxed ($Ctcf^{flox}$) mice, in which loxP sites flank exons 3–12, were previously reported.[25] The floxed allele occurs in the C57BL/6 background. To generate cardiac Ctcf cKO mice, we

crossed $Ctcf^{flox/flox}$ mice with transgenic mice expressing the α-myosin heavy chain promoter that directs expression of a tamoxifen-inducible Cre recombinase (MerCreMer).[26] Adult $Ctcf^{flox/flox}$ x α-MHC-$MCM^{+/-}$ mice (8 weeks) were administered tamoxifen (Tx) in the chow (0.4mg/g) for 5 weeks plus 1 week on normal chow to deplete CTCF.

Transverse Aortic Constriction and Echocardiographic Measurements

All animal studies were approved by the UCLA Animal Research Committee in compliance with the NIH Guide for the Care and Use of Laboratory Animals. Only adult mice were used in this study. Adult C57BL/6 male and female mice were subjected to transverse aortic constriction surgery to induce pressure overload and cardiac function was measured before, directly after and once every 5 days for the duration of the experiment as described.[27] Animals were sacrificed for experiments based on changes in ejection fraction and heart to body weight, indicating the presence of pathology.

Human Samples

All human samples used in this study were procured in the Ronald Reagan Medical Center at UCLA following patient consent according to IRB#11-001053-AM-00016. mRNA and protein were isolated from LVAD biopsy cores or explanted hearts using conventional approaches.

Electrophoresis and Western Blotting

Cardiomyocytes, neonatal rat ventricular myocytes or human heart tissue were lysed (50mM Tris pH 7.4/10mM ethylenediaminetetraacetic acid [EDTA]/1% Sodium dodecyl sulfate [SDS]/0.1mM phenylmethanesulfonylflouride/protease inhibitor cocktail pellet (Roche)/0.2mM sodium orthovanadate/ 0.1mM sodium fluoride/10mM sodium butyrate), sonicated, and separated via SDS-PAGE using Laemmli buffer. Detection was performed on the LI-COR odyssey. Antibodies were as follows: CTCF mix 1:500 (Abcam, ab70303), (Abcam, ab128909),

(BD, 612148), (Abiocode, R3171-1), (Diagenode, C15410210-50) and (Active Motif, 61311), H3K27me3 1:1000 (Abcam, ab6002), H3K4me3 1:1000 (Abcam, ab8580), Rad21 1:1000 (Abcam, ab992), GAPDH 1:1000 (Santa Cruz Biotechnology, sc20357), Actin 1:1000 (Santa Cruz Biotechnology, sc1616), secondaries 1:10,000 (LI-COR, IRDye conjugated). Relative quantification for CTCF expression normalized with respect to Actin was performed using ImageJ software.

RNA Isolation and qPCR

RNA from left ventricular adult cardiomyocytes were isolated using TRIzol (Thermo Fisher Scientific, 15596018) according to the manufacturer's protocol. cDNA was synthesized using iScript cDNA Synthesis Kit (Bio-Rad, 170-8891). qPCR was performed using SsoFast EvaGreen Supermix (Bio-Rad, 172-5201) on a BioRad, C1000 thermocycler.

SUPPLEMENTAL FIGURE LEGENDS

Supplemental Figure 1. Genome-wide chromatin conformation capture datasets and quality control analysis for Hi-C and RNA-seq. **(A)** Table summarizing read counts and mapping statistics for each sample type. Replicates of the same condition were combined upon verification that interactions and AB compartmentalization correlated with Pearson correlation > 0.90 (at 5kb resolution). **(B)** Coverage histograms of raw 5kb *cis* and *trans* matrices for each sample type (x axis indicates number of raw interactions and y axis indicates the number of bins that had such number of interactions). **(C)** Normalized interaction frequency per bin is highly conserved between biological replicates, Pearson correlation coefficient of > 0.95 in all comparisons. For this analysis, cis interactions ≤ 2Mb were compared. The normalized *cis* matrices were generated from ice-normalized *cis* and *trans* genome-wide matrices that were divided by matrix sum and multiplied by the arbitrary value of 1 million. **(D)** Summary statistics of RNA-seq sequencing data, including number of mapped read pairs for each sample.

Supplemental Figure 2. Generation and phenotypic characterization of cardiac-specific CTCF knockout mice. (A) Left, diagram showing the floxed *ctcf* gene from exon 3 to 12. Labeled yellow bars mark exons 1 to 12 and labeled green arrows indicate primers used to verify CTCF depletion via PCR. Primers p8563 and Skas1 should have a PCR product when exons 3 to 12 are excised by the Cre recombinase via the LoxP sites (blue triangles), and Primers p8563 and p8946 should have a PCR product in any scenario in which the Cre recombinase is not expressed. Right, α-MHC-Cre$^{+/-}$ x CTCF$^{flox/flox}$ mice were fed Tx containing chow (0.4mg Tx/g chow) for 5 weeks and then switched to normal chow for 1 week, resulting in deletion of exons 3-12 of CTCF. α-MHC-Cre$^{+/-}$ x CTCF$^{flox/flox}$ mice fed normal chow for 6 weeks, and α-MHC-Cre$^{+/-}$ x CTCF$^{WT/WT}$ mice fed tamoxifen chow for 5 weeks plus 1 week on normal chow, served as controls. **(B)** PCR genotyping confirms the presence of the floxed CTCF alleles

in our CTCF$^{flox/flox}$ Cre$^{+/-}$ mice (left), as well as presence of the *Cre* gene in these mice (center). After 5 weeks of tamoxifen treatment followed by 1 week on regular chow, gene excision in the heart was confirmed by PCR using p8563 and Skas1 primers (right). PCR amplified bands at ~500bp in the knockout (red arrows), but did not amplify the ~27kb region of the floxed allele in Cre$^{-/-}$ control mice (white arrows) or normal chow fed mice (black arrows). (Rg) regular chow. **(C)** CTCF KO was confirmed by RT-qPCR (left panel) for α-MHC-MCM$^{+/-}$ x CTCF$^{flox/flox}$ mice that were fed tamoxifen for 1, 2, 3, 4, 5 and 6 weeks. Blue bars show fold enrichment when compared to CTRL, and error bars indicate standard deviation; * indicates $p<0.05$ Student's t-test. **(D)** Kaplan-Meier survival curves of CTCF$^{flox/flox}$ Cre$^{+/-}$ (n=20) (red line), CTCF$^{wt/wt}$ Cre$^{+/-}$ (n=10) (green line), CTCF$^{flox/flox}$ Cre$^{-/-}$ (n=10) (blue line) fed with Tx and CTCF$^{flox/flox}$ Cre$^{+/-}$ (n=10) (orange line) fed with regular chow. Left panel, 5 weeks after Tx treatment, mouse survival decreased 63%, while survival dropped to 8% at 6 weeks. Right panel, Mouse survival stabilizes at 53% after the initial 5 weeks when mice are returned to normal chow. (Rg) regular chow. **(E)** RT-qPCR revealed mRNA down-regulation of SERCA (*Atp2a2*) and α-MHC (*Mhy6*), and upregulation of ANF (*Nppa*) and β-MHC (*Mhy7*), in mice undergoing 5 weeks Tx treatment plus 1 week regular chow (Rg). Bars show fold enrichment when compared to CTRL mouse given regular chow, and error bars indicate standard deviation; * indicates $p<0.05$ Student's t-test. **(F)** Western blot confirming CTCF depletion in tamoxifen-treated CTCF$^{flox/flox}$ Cre$^{+/-}$ mice (left), and showing no change in H3K27me3 and H3K4me3 with CTCF depletion. Quantification of average relative CTCF intensity shows a decrease in CTCF protein levels in CTCF$^{flox/flox}$ Cre$^{+/-}$ mice after 5 weeks of tamoxifen treatment. **(G)** Representative hematoxylin and eosin staining, comparing CTCF$^{wt/wt}$ Cre$^{+/-}$, CTCF$^{flox/flox}$ Cre$^{-/-}$and CTCF$^{flox/flox}$ Cre$^{+/-}$ after 5 weeks Tx treatment followed by 1 week on regular chow. CTCF$^{flox/flox}$ Cre$^{+/-}$ treated with regular chow for 6 weeks were used as an extra negative control while TAC samples were used as a positive control for disease. Considerable dilatation of the ventricles is observed in the tamoxifen-treated CTCF$^{flox/flox}$ Cre$^{+/-}$ mice as well as the TAC mice. *n* = 5 for each condition. (lv) left ventricle, (rv)

right ventricle, (Rg) regular chow. Scale bar: 1mm. **(H)** Echocardiographic measurements of all the mice used in the study. Notably, $CTCF^{flox/flox}$ $Cre^{+/-}$ mice treated with tamoxifen had a pathological phenotype when compared to the $CTCF^{flox/flox}$ $Cre^{+/-}$ or $CTCF^{wt/wt}$ $Cre^{+/-}$ that were given regular chow as well as the $CTCF^{wt/wt}$ $Cre^{+/-}$ or $CTCF^{flox/flox}$ $Cre^{-/-}$ mice treated with tamoxifen. *n* = 8-17 depending on the survival rate for each condition. Line indicates mean value for the parameter of interest while the error bars indicate standard deviation. (EF) ejection fraction, (LVIDd) LV internal diameter at diastole, (LVIDs) LV internal diameter at systole. **(I)** Representative B-mode (left) and M-mode (right) echocardiography images at 6 weeks from normal chow $CTCF^{flox/flox}$ Cre+/- (upper panel) or tamoxifen fed $CTCF^{wt/wt}$ $Cre^{+/-}$, $CTCF^{flox/flox}$ $Cre^{-/-}$ and $CTCF^{flox/flox}$ $Cre^{+/-}$ mice. $CTCF^{flox/flox}$ $Cre^{+/-}$ mice show pathological phenotype as in (H); a TAC mouse is shown for comparison.

Supplemental Figure 3. CTCF expression is down-regulated by pathologic stress and inversely correlated with heart size. (A) CTCF levels in mice undergoing a model of isoproterenol-induced heart failure across 87 genetically distinct strains. CTCF mRNA levels decrease across 80% of the mouse strains after isoproterenol treatment (top and middle panels; data from [28]). Cohesin subunit Smca1 shows coordinate regulation with CTCF in this model. **(B)** Phenotype data from 87 mouse strains treated with ISO are plotted against CTCF mRNA expression after ISO. Total heart mass, left ventricular mass, and right ventricular mass all show significant negative correlation with CTCF expression, while ejection fraction shows no correlation. p-values were calculated using the Pearson correlation coefficient. (LV) left ventricle, (RV) right ventricle (data from [28]). **(C)** Expression levels of different cohesin subunits decrease after CTCF depletion and TAC (log_{10}(FPKM+1).

Supplemental Figure 4. Cardiac disease associated genes differentially expressed after CTCF depletion. Real time qPCR measuring expression levels of different cardiac genes after 1, 2, 3, 4 and 5 weeks Tx treatment. Mice fed with regular chow (No Tx) and those fed with Tx were used as controls. Red and blue coloring indicates down- or up-regulation, respectively. (n=4/group; * $p<0.05$, Student's t-test).

Supplemental Figure 5. CTCF depletion does not promote apoptosis. Cleaved caspase-3 staining of heart sections from CTRL and CTCF KO mice. Human sarcoma tumor cells were used as a positive control (Right panel).

Supplemental Figure 6. Human subject clinical data. Available data on patients from whom heart samples were obtained is provided. "Wb quantitation" is the CTCF protein level measured by Western blot expressed as a ratio of after to before LVAD. NICM, non-ischemic cardiomyopathy; ICM, ischemic cardiomyopathy; NYHA, New York Heart Association Classification; EF, ejection fraction at time of LVAD placement.

Supplemental Figure 7. Differences in boundary strength and A/B compartmentalization per chromosome. (A) Boundary strength differences between groups (red, higher; blue, lower; Insets: example region on chromosome 16. **(B)** Percent of genome-wide A/B compartment change with CTCF depletion (left) and TAC (right). Bottom panels highlight only bins that change compartment.

Supplemental Figure 8. Implications for cardiac phenotype from chromatin structural changes in TAC and CTCF-KO cardiac myocytes. (A) Principal component analysis of the shared insulation boundary strengths. **(B)** Number of new boundaries between different experimental groups. Analyses do not distinguish between boundaries that emerge either from

shifting of an existing boundary outside the analysis window (+/-5kb from CTRL boundary center) or *de novo* formation of a completely new boundary. Color codes: Boundaries only found in CTRL (blue), only found in perturbation (beige), and shared between CTRL and perturbation (pink). **(C)** Principal component analysis of the RNA-seq samples. Control separates from CTCF KO and TAC on PC1. **(D)** KEGG pathway analysis of up-regulated (top) or down-regulated (bottom) genes bound by CTCF. Terms highlighted in green are cardiac-related. **(E)** KEGG pathway analysis of genes (2570; Figure 3F) that lie within the loops that lose $\geq$1 CTCF peak in CTCF-KO. **(F)** KEGG pathway analysis of genes (Figure 3H, "lost loops") that lie within the 151 enhancer-promoter loops that are lost in CTCF-KO (left), the 174 lost with TAC (middle), and the 114 loops lost in both diseased conditions (CTCF-KO and TAC; right). **(G)** KEGG pathway analysis of the differentially expressed genes (Figure 5C, "enhancers with decrease in interactions") interacting with enhancers that lose interactions after perturbation (left, control vs. CTCF-KO; middle, control vs. TAC; right, shared).

REFERENCES

1. Rao SS, Huntley MH, Durand NC, Stamenova EK, Bochkov ID, Robinson JT, Sanborn AL, Machol I, Omer AD, Lander ES and Aiden EL. A 3D map of the human genome at kilobase resolution reveals principles of chromatin looping. *Cell*. 2014;159:1665-1680.
2. Li H and Durbin R. Fast and accurate short read alignment with Burrows-Wheeler transform. *Bioinformatics*. 2009;25:1754-1760.
3. Schmitt AD, Hu M, Jung I, Xu Z, Qiu Y, Tan CL, Li Y, Lin S, Lin Y, Barr CL and Ren B. A Compendium of Chromatin Contact Maps Reveals Spatially Active Regions in the Human Genome. *Cell Rep*. 2016;17:2042-2059.
4. Imakaev M, Fudenberg G, McCord RP, Naumova N, Goloborodko A, Lajoie BR, Dekker J and Mirny LA. Iterative correction of Hi-C data reveals hallmarks of chromosome organization. *Nat Methods*. 2012;9:999-1003.
5. Crane E, Bian Q, McCord RP, Lajoie BR, Wheeler BS, Ralston EJ, Uzawa S, Dekker J and Meyer BJ. Condensin-driven remodelling of X chromosome topology during dosage compensation. *Nature*. 2015;523:240-244.
6. Servant N, Varoquaux N, Lajoie BR, Viara E, Chen CJ, Vert JP, Heard E, Dekker J and Barillot E. HiC-Pro: an optimized and flexible pipeline for Hi-C data processing. *Genome Biol*. 2015;16:259.
7. Bolstad BM, Irizarry RA, Astrand M and Speed TP. A comparison of normalization methods for high density oligonucleotide array data based on variance and bias. *Bioinformatics*. 2003;19:185-193.
8. Durand NC, Shamim MS, Machol I, Rao SS, Huntley MH, Lander ES and Aiden EL. Juicer Provides a One-Click System for Analyzing Loop-Resolution Hi-C Experiments. *Cell Syst*. 2016;3:95-98.
9. Durand NC, Robinson JT, Shamim MS, Machol I, Mesirov JP, Lander ES and Aiden EL. Juicebox Provides a Visualization System for Hi-C Contact Maps with Unlimited Zoom. *Cell Syst*. 2016;3:99-101.
10. Lun AT, Perry M and Ing-Simmons E. Infrastructure for genomic interactions: Bioconductor classes for Hi-C, ChIA-PET and related experiments. *F1000Res*. 2016;5:950.
11. Ay F, Bailey TL and Noble WS. Statistical confidence estimation for Hi-C data reveals regulatory chromatin contacts. *Genome Res*. 2014;24:999-1011.
12. Yin T, Cook D and Lawrence M. ggbio: an R package for extending the grammar of graphics for genomic data. *Genome Biol*. 2012;13:R77.
13. Kim D, Pertea G, Trapnell C, Pimentel H, Kelley R and Salzberg SL. TopHat2: accurate alignment of transcriptomes in the presence of insertions, deletions and gene fusions. *Genome Biol*. 2013;14:R36.
14. Trapnell C, Williams BA, Pertea G, Mortazavi A, Kwan G, van Baren MJ, Salzberg SL, Wold BJ and Pachter L. Transcript assembly and quantification by RNA-Seq reveals unannotated transcripts and isoform switching during cell differentiation. *Nature biotechnology*. 2010;28:511-515.
15. Trapnell C, Hendrickson DG, Sauvageau M, Goff L, Rinn JL and Pachter L. Differential analysis of gene regulation at transcript resolution with RNA-seq. *Nature biotechnology*. 2013;31:46-53.

16. Goff L, Trapnell C and Kelley D. cummeRbund: Ananlysis, exploration, manipulation and visualization of Cufflinks high-throughput sequencing data. *R package version 2160*. 2013;https://bioconductor.org/packages/release/bioc/html/cummeRbund.html.
17. Monte E, Rosa-Garrido M, Karbassi E, Chen H, Lopez R, Rau CD, Wang J, Nelson SF, Wu Y, Stefani E, Lusis AJ, Wang Y, Kurdistani SK, Franklin S and Vondriska TM. Reciprocal Regulation of the Cardiac Epigenome by Chromatin Structural Proteins Hmgb and Ctcf: IMPLICATIONS FOR TRANSCRIPTIONAL REGULATION. *J Biol Chem*. 2016;291:15428-15446.
18. Langmead B and Salzberg SL. Fast gapped-read alignment with Bowtie 2. *Nat Methods*. 2012;9:357-359.
19. Li H, Handsaker B, Wysoker A, Fennell T, Ruan J, Homer N, Marth G, Abecasis G, Durbin R and Genome Project Data Processing S. The Sequence Alignment/Map format and SAMtools. *Bioinformatics*. 2009;25:2078-2079.
20. Zhang Y, Liu T, Meyer CA, Eeckhoute J, Johnson DS, Bernstein BE, Nusbaum C, Myers RM, Brown M, Li W and Liu XS. Model-based analysis of ChIP-Seq (MACS). *Genome Biol*. 2008;9:R137.
21. Yu G, Wang LG and He QY. ChIPseeker: an R/Bioconductor package for ChIP peak annotation, comparison and visualization. *Bioinformatics*. 2015;31:2382-2383.
22. Shen L, Shao N, Liu X and Nestler E. ngs.plot: Quick mining and visualization of next-generation sequencing data by integrating genomic databases. *BMC genomics*. 2014;15:284.
23. Carlson M. KEGG.db: A set of annotation maps for KEGG. *R package version 323*. 2016;http://bioconductor.org/packages/release/data/annotation/html/KEGG.db.html.
24. O'Connell TD, Rodrigo MC and Simpson PC. Isolation and culture of adult mouse cardiac myocytes. *Methods Mol Biol*. 2007;357:271-296.
25. Heath H, Ribeiro de Almeida C, Sleutels F, Dingjan G, van de Nobelen S, Jonkers I, Ling KW, Gribnau J, Renkawitz R, Grosveld F, Hendriks RW and Galjart N. CTCF regulates cell cycle progression of alphabeta T cells in the thymus. *Embo J*. 2008;27:2839-2850.
26. Sohal DS, Nghiem M, Crackower MA, Witt SA, Kimball TR, Tymitz KM, Penninger JM and Molkentin JD. Temporally regulated and tissue-specific gene manipulations in the adult and embryonic heart using a tamoxifen-inducible Cre protein. *Circ Res*. 2001;89:20-25.
27. Franklin S, Chen H, Mitchell-Jordan S, Ren S, Wang Y and Vondriska TM. Quantitative analysis of the chromatin proteome in disease reveals remodeling principles and identifies high mobility group protein B2 as a regulator of hypertrophic growth. *Mol Cell Proteomics*. 2012;11:M111 014258.
28. Rau CD, Wang J, Avetisyan R, Romay M, Ren S, Wang Y and Lusis AJ. Mapping genetic contributions to cardiac pathology induced by beta-adrenergic stimulation in mice. *Circulation Cardiovascular Genetics*. 2015;8:40-49.

A)

					Intrachromosomal reads				Interchromaosomal reads				
Treatment Group	Raw Read Count	Mapped Reads	% mapped	Monoclonal Reads	cis	% cis	cis > 15kb	% cis >15kb	trans	% trans	Est Lig. Efficiency	Cis:Trans	Fraction usable
Control	1,356,986,441	861,270,542	63%	761,834,590	467,423,206	61%	302,126,321	65%	294,411,384	39%	78%	1.6	40%
CTCF KO	1,322,639,616	858,967,104	65%	790,475,662	537,778,393	68%	362,715,416	67%	252,697,269	32%	78%	2.1	46%
TAC	1,264,314,812	812,152,976	64%	753,020,109	452,438,115	60%	311,577,542	69%	300,581,994	40%	81%	1.5	41%

B)

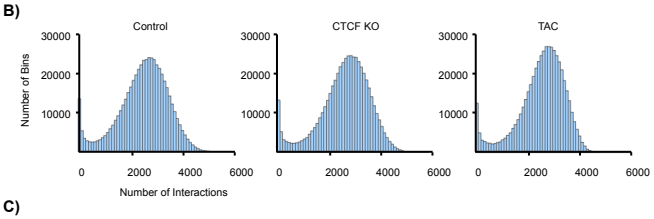

Sample	≥ 1000 interactions	Total bins	%
Control	473993	526765	89.9
CTCF KO	476943	526765	90.5
TAC	477245	526765	90.5

C)

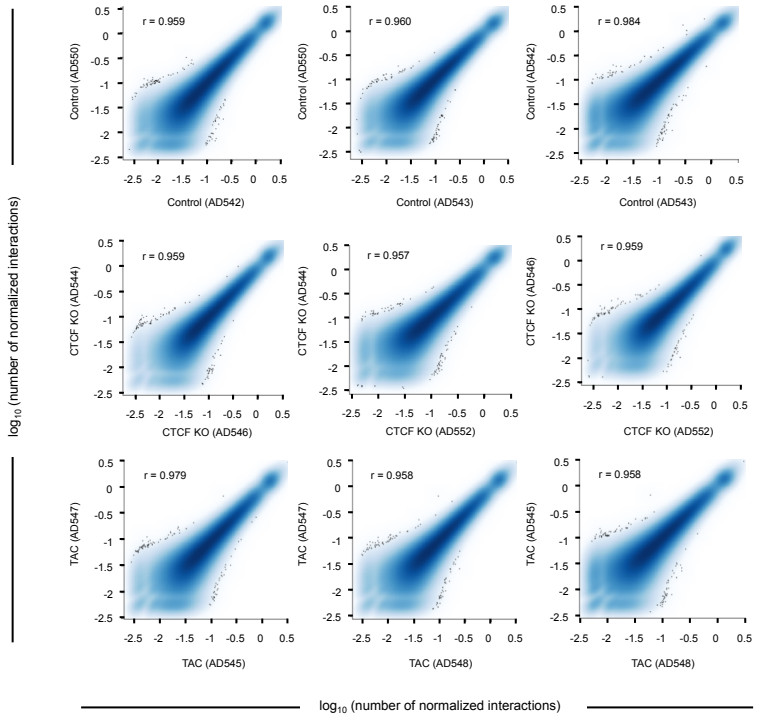

D)

Barcode	Sample	Mouse	Raw Pairs	Mapped Pairs	Percent Mapped	Discordant Pairs	New Percent Mapped	Percent reported by TopHat
BC12	2689	Control	62678103	47580789	0.759129373	113785	0.757313986	75.7%
BC13	2673	Control	57132693	42640436	0.746340383	84326	0.744864416	74.5%
BC7	2675	Control	71206543	53260200	0.747967782	168068	0.745607493	74.6%
BC1	2722	CTCF KO	44735724	33536481	0.749657723	154258	0.746209517	74.6%
BC3	2713	CTCF KO	43628085	31889931	0.730949594	182662	0.726762795	72.7%
BC8	2709	CTCF KO	56190815	41561052	0.739641381	180738	0.736424877	73.6%
BC9	2714	CTCF KO	51869564	39252526	0.756754501	176576	0.753350269	75.3%
BC2	2754	TAC	64162171	47786649	0.744779178	168931	0.742146303	74.2%
BC10	2761	TAC	48135253	36064672	0.749236158	130495	0.746525151	74.7%
BC11	2755	TAC	80658101	59548603	0.738284218	224236	0.735504137	73.6%

Supplemental Figure 1.

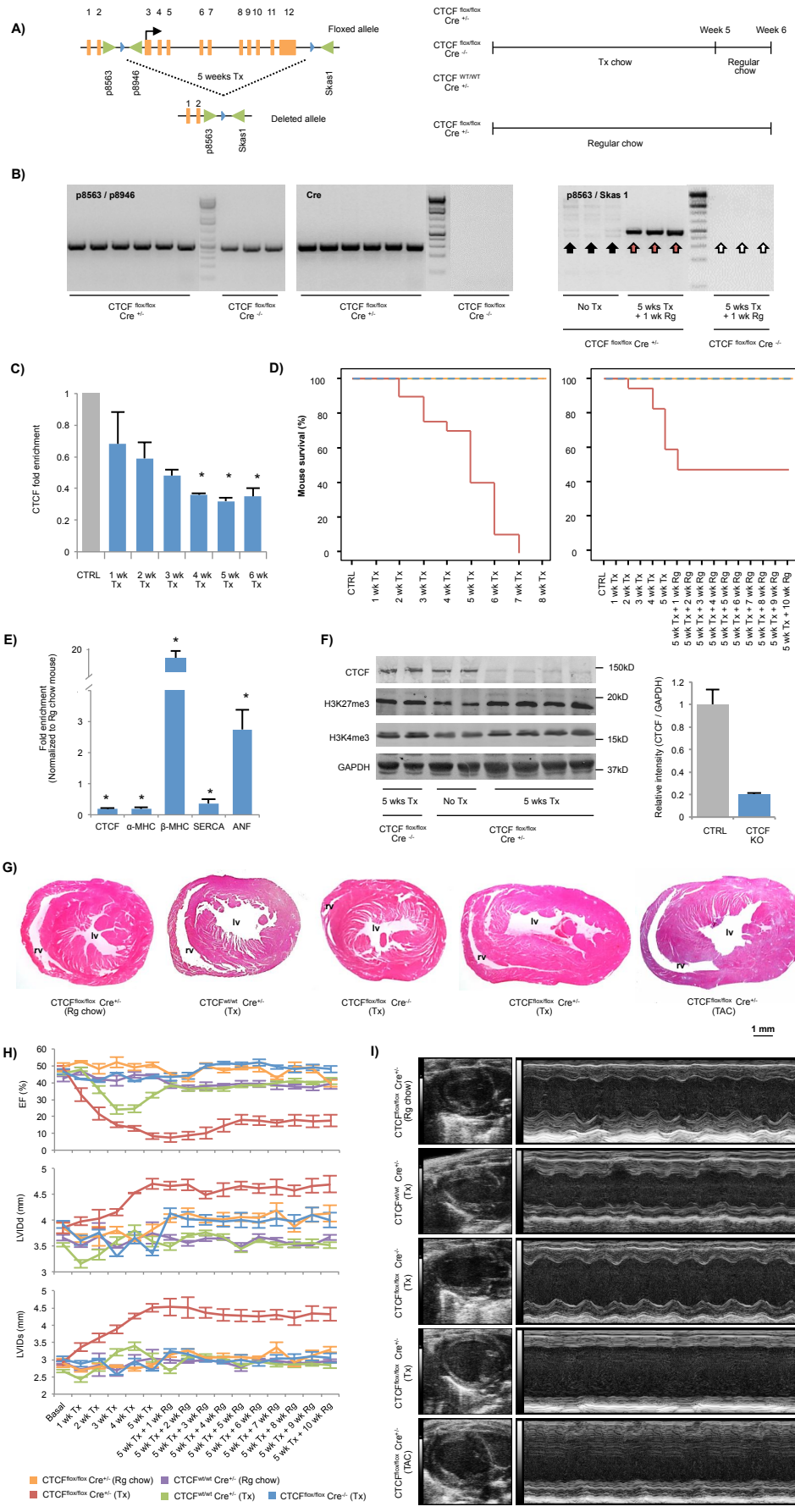

Supplemental Figure 2.

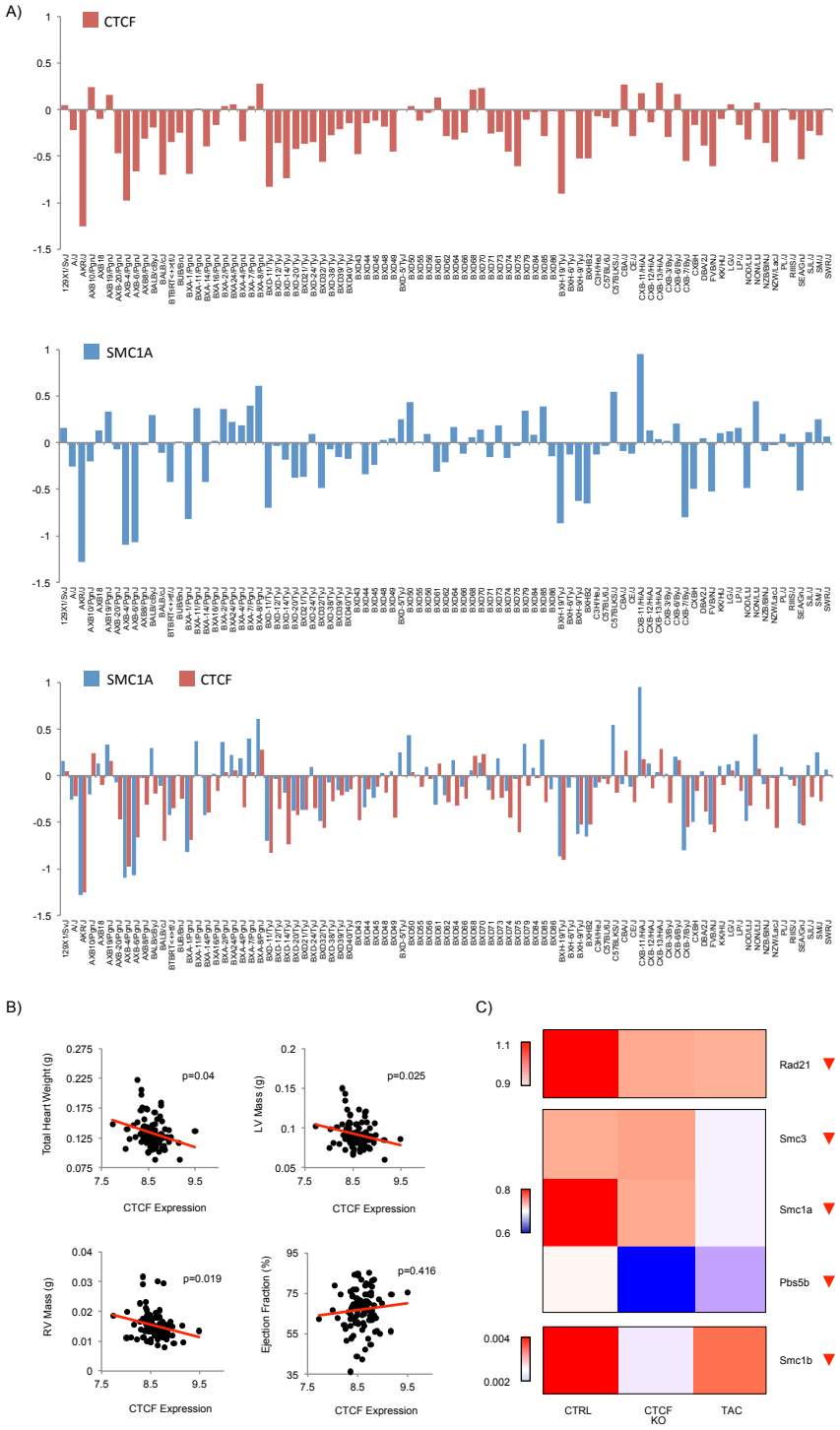

Supplemental Figure 3.

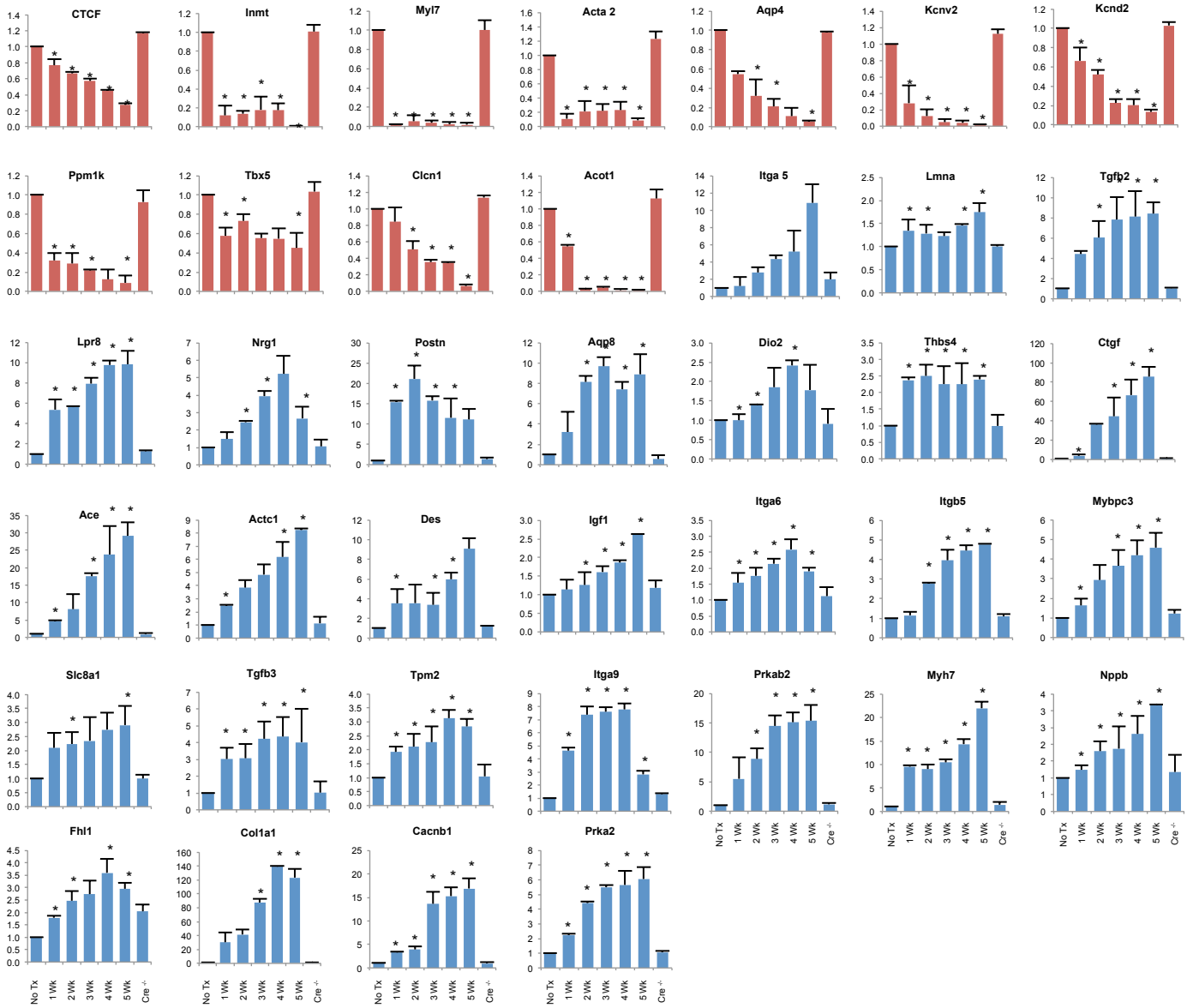

Supplemental Figure 4.

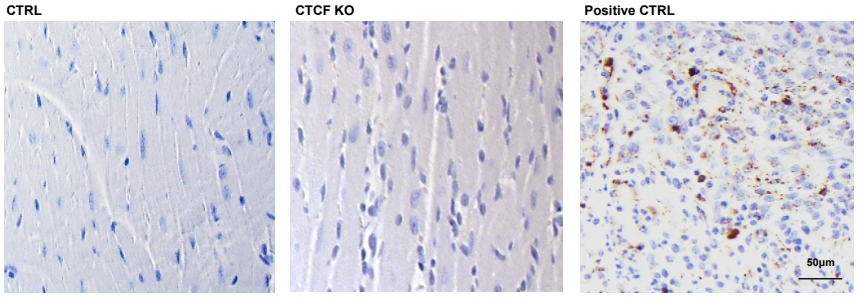

Supplemental Figure 5.

Sample	Management	Sex	Age (Year)	Etiology	EF	Wb quantification (After / Before)	LVEDD (mm)	NYHA class	BNP (pg/mL)	Comorbidities	Medical History	Medications
114	Before LVAD	Male	43	NICM	25	2.12	69	4	402	None noted	Dyslipidemia Atrial fibrillation	Pravastatin Cardizem
119	After LVAD (7 weeks)						45	2	73			
167	Before LVAD	Male	55	NICM	20	2.54	70	4	778	COPD due to 50 years of smoking history	Adenoidectomy Non sustained ventricle tachycardia Heparin induced thrombocytopenia	Amiodarone Epinephrine Alteplase
177	After LVAD (8 weeks)						45	2	59			
141	Before LVAD	Male	65	ICM	20	1.14	65	4	548	STEMI Type 2 DM	Arthritis Hypertension Coronary artery disease	Amlodipine Atorvastatin Hydralazine Metoprolol Sildenafil Spironolactone Warfarin
161	After LVAD (24 weeks)						40	2	57			
117	Before LVAD	Male	55	ICM	20	1.12	68	3B	402	Type 2 DM Renal insufficiency Dyslipidemia	Hypertension Acute Pancreatitis Colitis	Amlodipine Furosemide Pravastatin
181	After LVAD (51 weeks)						42	2	66			

Supplemental Figure 6.

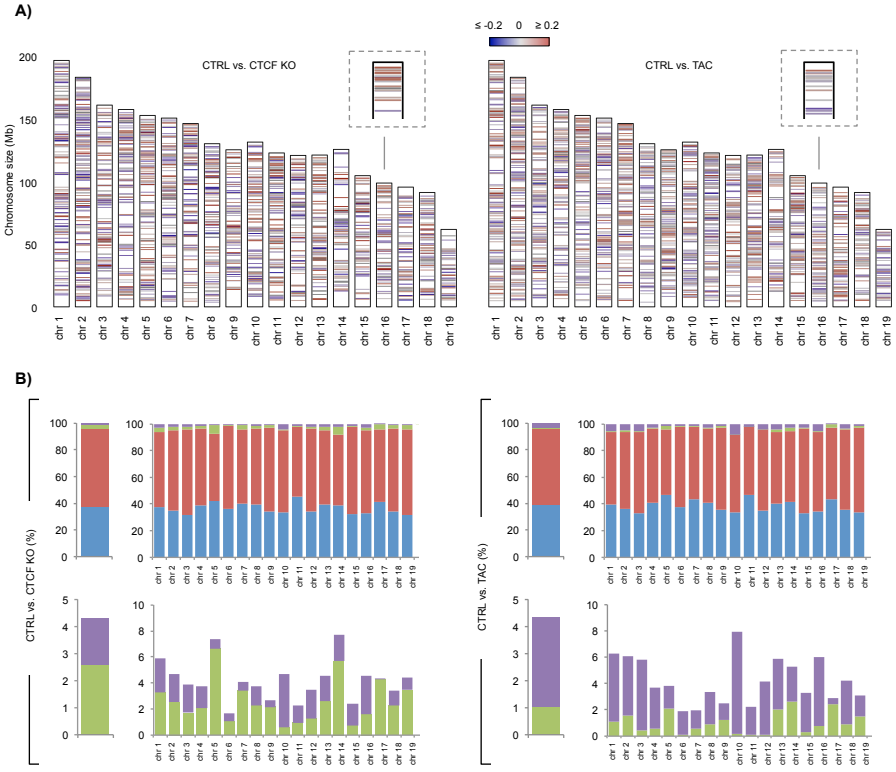

Supplemental Figure 7.

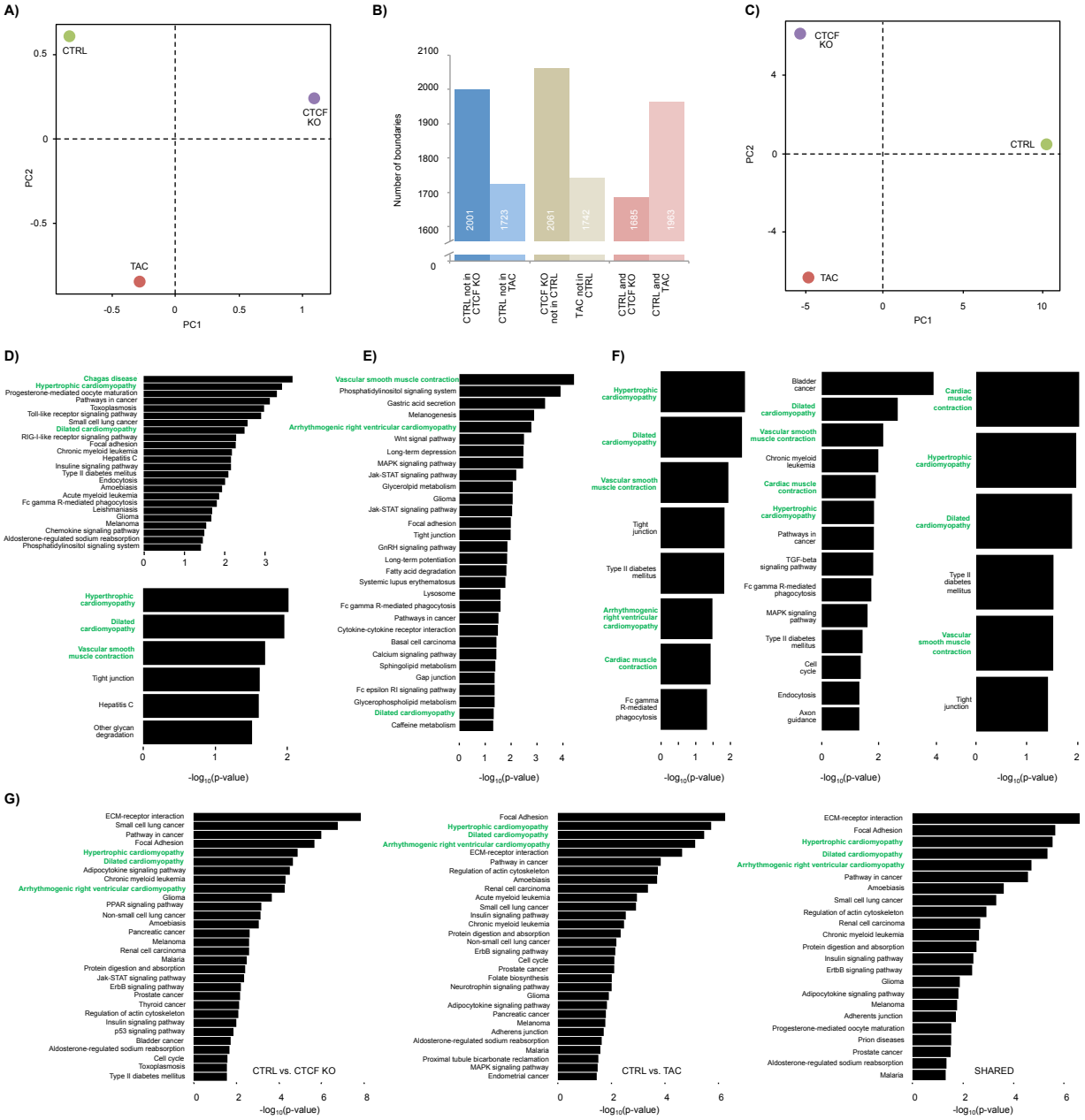

Supplemental Figure 8.